Structural and Multidisciplinary Optimization (2025) 68:120
https://doi.org/10.1007/s00158-025-04050-7

RESEARCH PAPER

Adjoint-assisted robust shape optimization of an idealized arterial bypass graft using the FOSM method

Georgios Bletsos[1] · **Lars Radtke**[2] · **Thomas Rung**[1]

Received: 11 November 2024 / Revised: 14 May 2025 / Accepted: 23 May 2025

Abstract

This paper presents the shape optimization of an idealized arterial bypass graft under uncertainties. The underlying blood flow problem is numerically solved using computational fluid dynamics (CFD) simulations, able to account for mechanical hemolysis and non-Newtonian viscosity properties of blood. The employed hemolysis and non-Newtonian models utilize a set of parameters that are considered uncertain in this work. To this end, the optimization problem is rendered robust and targets the minimization of the first two statistical moments of a hemolysis index. The propagation of the uncertainties to the hemolysis index is done through the first-order second-moment method (FOSM). The necessary derivatives are computed by the adjoint method and finite differences. Several steady-state robust shape optimization simulations of the idealized bypass graft are presented. Selected optimized shapes are further assessed by means of additional fluid–structure interaction (FSI) simulations under unsteady conditions.

Keywords Adjoint-based shape optimization · Robust shape optimization · First-order second-moment method · Hemodynamics · Bypass-graft · Hemolysis

1 Introduction

Simulation-driven shape optimization procedures have for several years been studied and applied in a wide range of engineering applications. Most of the designs produced today in automotive, maritime, and aeronautics industries have undergone a certain level of optimization, based on either computational fluid dynamics (CFD) or computational structural mechanics (CSM) simulations. The industrial interest on the field of shape optimization is concurrently accompanied by a significant research effort, see, e.g., Katsapoxaki et al. (2023), Kühl et al. (2022), Upadhyay et al. (2021), Papoutsis-Kiachagias et al. (2019) for some recent publications. The success of such methods in the aforementioned industries naturally raises the question of their applicability in biomedical applications (Marsden 2014). This paper aims to present how several aspects of an optimization method, that are considered established in most fields of engineering interest, can be successfully applied in a biomedical context.

In shape optimization, one searches for the optimal configuration of a domain, so that an *objective functional* is minimized. A wide variety of optimization methods, ranging from stochastic (or global) (Bäck 1996) to deterministic (or local) (Nocedal and Wright 2006) exists. The decision upon the employment of a specific method depends on the design task and underlying problem. On the one hand, global techniques, such as evolutionary algorithms (Jahangirian and Shahrokhi 2011; Giannakoglou et al. 2006), are able to provide the global optimum, as the name suggests, given that a large number of candidate solutions are evaluated. This option is attractive for non-convex problems and cheap evaluation methods but becomes computationally unfeasible for a large number of control variables and/or expensive evaluation methods. On the other hand, deterministic strategies are able to arrive at a local minimum using the information of the gradient of the objective functional with respect to

---

Responsible editor: Seonho Cho

✉ Georgios Bletsos
george.bletsos@tuhh.de

[1] Institute for Fluid Dynamics and Ship Theory (M-8), Hamburg University of Technology, Am Schwarzenberg-Campus 1, 21073 Hamburg, Germany

[2] Institute for Ship Structural Design and Analysis (M-10), Hamburg University of Technology, Am Schwarzenberg-Campus 1, 21073 Hamburg, Germany

(w.r.t.) the control, i.e., the shape. These approaches, frequently referred to as gradient-based methods, require support from a tool able to compute the desired gradient. The computation of the gradient is a crucial step that can be realized by several different approaches (Martins and Hwang 2013). Depending on the approach for obtaining the sought gradient, the computational cost of the optimization method can significantly vary. For most applications in the literature, the *adjoint method* has been the method of choice for the computation of the sought gradient due to its computational efficiency for problems of many control variables, see e.g., Kühl et al. (2019), Papoutsis-Kiachagias and Giannakoglou (2016), Bletzinger (2014), Stück and Rung (2013), Othmer (2008), Brezillon and Gauger (2004).

Regardless of the optimization process to be followed, most of the commonly available methods require the computational modeling of the underlying physical problem. In the case of biomedical applications, this often refers to the numerical solution of blood flows. Numerical simulations based on continuum mechanics can sufficiently describe the flow of blood in an extensive range of applications; see, e.g., Quarteroni et al. (2000) for a review on computational vascular fluid dynamics. The goal of simulating such flows, that within this paper will be referred to as *the primal problem*, is to predict hemodynamic quantities of interest (QoI). This work considers mechanical hemolysis[1] to be the primary QoI. Hemolysis refers to the mechanical damage of red blood cells (RBCs) and the release of their contents, predominantly hemoglobin, in the blood plasma due to excessively high stress induced by peculiarities of the blood flow. Hemolysis induction is usually encountered in biomedical devices, where large velocity gradients are found, e.g., blood pumps (Yu et al. 2016; Thamsen et al. 2015), but it can also appear *in vivo* conditions, i.e., in a living person, when vessels delivering blood are kinked or stenosed (Goubergrits et al. 2018). Several computational hemolysis prediction models have been developed and successfully coupled with CFD solvers; see, e.g., Yu et al. (2017) for a review on the topic.

Furthermore, a usual practice in CFD simulations of hemodynamics is to model blood as a Newtonian fluid. While this assumption has been shown to sufficiently describe the rheology of blood in flows exposed to high shear rates, it falls short in flows of low shear rates due to the shear-thinning behavior of blood (Fung 1993). Several non-Newtonian models have been proposed to deal with this inadequacy and account for pseudo-plastic behavior (Quarteroni et al. 2000). Even though most of the available non-Newtonian models cannot account for viscoelastic properties, they can still provide significant information with a small implementation effort into a CFD framework.

An additional aspect of recent biomedical interest is the interaction of blood with a solid surface, which exhibits an increased elasticity. It has been shown that the rigid wall assumption of a classical CFD simulation has in many cases proven to be inadequate to accurately predict certain blood flow problems; see e.g., Hsu et al. (2014), Bazilevs et al. (2010). To this end, extensive focus has recently been given to fluid–structure interaction (FSI) simulations that consider the fluid flow and the displacement of the vessel wall in a coupled manner. A general overview of cardiovascular FSI can be found in Bazilevs et al. (2013).

When a computational model of the physical problem is available, it is common practice to assume precise knowledge of the conditions under which a flow phenomenon occurs. This is, however, rarely the case. Frequently, it is observed that the initial assumption of accurate knowledge is only a coarse approximation, with the actual values fluctuating around what was initially assumed to be precise. If this assumption is employed on a shape optimization procedure, a shape that is considered to be optimal for one application is sometimes proven below par in reality due to the uncertain nature of the conditions under which the application occurs. This led to the emergence of the field of *robust shape optimization* which aims to identify an optimal solution out of a range of probable conditions. To include the uncertainties in the optimization problem, the uncertain variables, which could refer to, e.g., modeling parameters, boundary conditions, or initial conditions, are considered to follow statistical distributions and are described based on their mean and standard deviation. To this extent, the QoI, that in traditional shape optimization refers to a deterministic quantity, is now affected by the randomness of the uncertain variables and also acts as a statistical quantity, characterized by its statistical moments. The optimization is then usually formulated as the minimization of functionals combining these moments, depending on the design task. The identification of the statistical moments of the QoI is referred to as Uncertainty Quantification (UQ). The most straightforward strategies for UQ refer to Monte Carlo (MC) (Janssen 2013) or MC-based methods (Chatterjee et al. 2019; Morokoff and Caflisch 1995), where the simulation of an excessive number of realizations, i.e., specific outcomes of the random process, is required. To avoid the computationally intensive simulation of several realizations, the Method of Moments (MoM) has been proposed as a suitable alternative for UQ (Kranz et al. 2023; Papadimitriou and Giannakoglou 2013). The MoM is based on a Taylor series expansion of the QoI around the mean values of the uncertain variables and can provide the sought statistical moments with the use of derivatives of the QoI w.r.t. the uncertain variables. The

---

[1] For the sake of brevity, the word *mechanical* might be omitted throughout this paper. In all instances, reference to hemolysis stands for mechanical hemolysis.

first-order second-moment (FOSM) method truncates the expansion after the first-order term. It is worth noting that the FOSM method requires no assumption on the type of distribution of the uncertain parameters (Kriegesmann and Lüdeker 2019).

In this paper, we present the gradient-based robust shape optimization of an idealized bypass graft, frequently used in surgical procedures as an alternative route around severely stenosed arteries. Studies such as those of Jiang et al. (2016) and Zhang and Liu (2015) have previously investigated the deterministic shape and topology optimization, respectively, of idealized two-dimensional bypass configurations using the level-set method in combination with adjoint techniques for the minimization of a blood damage-related metric. In both studies, significant improvements were identified as compared to initial configurations, highlighting the potential of formal optimization techniques for arterial graft design. It is also worth noting the recent study of Habibi et al. (2025), in which an automatic multi-objective Bayesian shape optimization was built for patient-specific vascular grafts. Similarly to the present work, the authors of Habibi et al. (2025) built their optimization framework based on steady-state CFD simulations and later assessed their designs on transient simulations, under the rigid wall assumption. They noted that in most of the cases, the steady-state produced shapes also showed superior results when assessed by transient simulations. The optimization procedure followed in this work considers the control to be the complete three-dimensional shape of the graft and host artery, in a CAD-free manner (Radtke et al. 2023). Modeling parameters for the estimation of hemolysis (3 parameters) and non-Newtonian viscosity (4 parameters) are considered uncertain, cf. Eq. (8). The optimization targets the minimization of the convex combination of the first two statistical moments of the QoI. Shape sensitivities are computed using the continuous adjoint method, developed and presented in Bletsos et al. (2023, 2021). The MoM is employed for the UQ of the problem. Select optimized shapes are subsequently assessed by means of a partitioned FSI approach.

The remainder of this paper is organized as follows: In Sect. 2, we present the numerical methodology employed for the solution of the robust shape optimization problem. Specifically, we describe each step of the process as well as numerical aspects to arrive at the necessary quantities for optimization. The section closes with the presentation of the complete optimization algorithm. Section 3 is concerned with the application of the presented methodology on the idealized bypass graft geometry. We perform five optimization runs by combining different uncertain parameters and weights in the definition of the robust objective functional. Two selected designs are further evaluated under FSI conditions. The paper closes with conclusions and outlines future work directions in Sect. 4. In “Appendix A”, we briefly describe the FSI methodology employed in this work. “Appendix B” presents core aspects of the derivation process of the continuous adjoint system employed in this work and a verification study for the proposed adjoint sensitivity expression. “Appendix C” presents a sensitivity analysis study w.r.t. the uncertain parameters.

Throughout the paper, Einstein’s summation convention applies for repeated lower-case Latin subscripts. Vectors and higher-order tensors are defined with reference to Cartesian coordinates.

2 Methodology

This section is dedicated to the presentation of key aspects of the numerical method employed in this work. Specifically, we present the primal problem and discuss its numerical solution using CFD. The primal problem is subsequently considered uncertain by means of its parameters and we discuss the UQ method followed to identify the statistical moments of the QoI. The section closes with the presentation of the robust shape optimization problem in the framework of a CAD-free gradient-based optimization approach.

2.1 Blood flow modeling

In what follows, we refer to the fluid domain as Ω and its boundary as Γ. Furthermore, we distinguish segments of the boundary as inlet, Γ_{in}, outlet Γ_{out}, and wall Γ_{w}, with $\Gamma = \Gamma_{\text{in}} \cup \Gamma_{\text{out}} \cup \Gamma_{\text{w}}$. We model blood as an incompressible, non-Newtonian fluid and the flow as laminar and steady-state. The equations of state are thus described based on the conservation of mass and momentum in Ω, viz.

$$R^p = -\frac{\partial v_i}{\partial x_i} = 0 \tag{1}$$

$$R_i^v = \rho v_j \frac{\partial v_i}{\partial x_j} - \frac{\partial}{\partial x_j}\left(2\tilde{\mu} S_{ij} - p\delta_{ij}\right) = 0, \tag{2}$$

where R^p and R_i^v refer to the residual forms of the continuity and momentum equations, respectively. We denote with x_i the Cartesian spatial coordinate, $\rho = 1056\,\mathrm{kg/m^3}$ denotes the fluid’s density, v_i the Cartesian velocity components, p the pressure, $S_{ij} = 0.5\left(\partial v_i/\partial x_j + \partial v_j/\partial x_i\right)$ the strain-rate tensor components, and δ_{ij} the Kronecker delta components. The effective viscosity of the non-Newtonian fluid is given based on a non-linear relation to the second invariant of the strain-rate tensor, which we define as

$$\dot{\gamma} = \sqrt{2S_{ij}S_{ij}}. \tag{3}$$

In this work, we employ the Carreau model to describe this relation, viz.

$$\tilde{\mu} = \mu_\infty + (\mu_0 - \mu_\infty)(1 + (\lambda\dot{\gamma})^2)^{\frac{n-1}{2}}, \tag{4}$$

where λ, n, μ_0, and μ_∞ are considered as parameters of the model. The Carreau model appears to be one of the most suitable choices for the investigations conducted in this study, as it effectively supports the continuous adjoint calculus and spans a broad range of viscosity values. However, it must be noted that the choice of the non-Newtonian viscosity model is not restrictive and other models able to describe the shear-thinning nature of blood, such as the Power-law (Shibeshi and Collins 2005), Casson law (Blair 1959), and modified Cross model (Zhang and Liu 2015), could be used.

Equations (1, 2, 4) describe the flow of blood. In addition to this, we also model hemolysis based on a typical power-law hemolysis prediction model, which is one-way coupled to the flow equations (Garon and Farinas 2004; Giersiepen et al. 1990). The one-way coupling implies that information from the solution of the flow dynamics are used by the hemolysis model with no subsequent retroaction to them. In an Eulerian framework, this can be written as

$$R^H = v_j \frac{\partial H_L}{\partial x_j} - C^{\frac{1}{\beta}} \bar{\tau}^{\frac{\alpha}{\beta}} \left(1 - H_L\right) = 0 \qquad \text{in} \quad \Omega, \tag{5}$$

where $H_L = H^{\frac{1}{\beta}}$ is the unknown variable and H denotes a local measure for the released hemoglobin to the total hemoglobin within an RBC. Hemolysis induction is governed by shear stresses and the model is driven by $\bar{\tau}$ that is based on the second invariant of the stress tensor, viz.

$$\bar{\tau} = \sqrt{-\frac{1}{2}\left(\mathrm{tr}(\tau_{ij})^2 - \mathrm{tr}(\tau_{ij}^2)\right)} \quad \text{with} \quad \tau_{ij} = 2\tilde{\mu}S_{ij}. \tag{6}$$

It is noted that for an incompressible fluid $\mathrm{tr}(\tau_{ij}) \sim \partial v_i/\partial x_i$ and thus disappears on a converged state of the flow. The model is closed by a set of parameters (C, α, β).

Once the flow solution and distribution of H_L is known, a QoI that measures the hemolysis induction potential of the flow can be computed. A usual metric for this QoI is a hemolysis index that measures the mass-flow-average of hemolysis on the outlet of the computational domain

$$F = \frac{\int_{\Gamma_{\text{out}}} H v_i n_i \, \mathrm{d}\Gamma}{\int_{\Gamma_{\text{out}}} v_i n_i \, \mathrm{d}\Gamma}. \tag{7}$$

The boundary conditions employed to close the flow and hemolysis problem are as follows:

- Dirichlet velocity and hemolysis and zero Neumann pressure on Γ_{in},
- Dirichlet velocity and zero Neumann pressure and hemolysis on Γ_{w},
- Dirichlet pressure and zero Neumann velocity and hemolysis on Γ_{out}.

The numerical solution of the primal problem is based on the finite volume method employed by the in-house software *FreSCo*$^+$ (Rung et al. 2009). For the solution of Eqs. (1, 2), the segregated algorithm employs the SIMPLE method for pressure–velocity coupling. A collocated storage arrangement is employed for all transport quantities and parallelization is possible by means of domain decomposition (Yakubov et al. 2013). For the non-Newtonian fluid model employed in this work, the non-linear relation of the effective viscosity to the strain-rate tensor, cf. Eq. (4), introduces an additional non-linearity to the momentum equations. This is resolved in our numerical scheme based on a Picard-like linerization approach, in which the effective viscosity is evaluated at each cell center based on the velocity of the previous pressure–velocity coupling iteration. The face-based values of viscosity required for the discretization of the diffusive term are obtained based on a linear interpolation from the adjacent cells. Once Eqs. (1, 2) are solved, Eq. (5) can be solved in a straightforward manner using similar discretization techniques. In this work, the higher-order QUICK scheme is used to discretize all convective terms.

For the FSI simulations considered in this work, the fluid solver needs to be coupled to a structural solver. Key aspects of the partitioned solution approach followed for FSI in this work are presented in “Appendix A”. The interested reader is pointed to Bletsos et al. (2024) for detailed information.

2.2 Uncertainty quantification based on the MoM

The parameters employed by the hemolysis and non-Newtonian models are typically deduced from fitting models to experimental data. Although experiments are conducted under well-controlled conditions, the same parameter sets are frequently used for more complex computational studies. Furthermore, it is often the case that experimental studies result in a different fitting of the same models thus proposing a different set of parameters; see, e.g., Zhang et al. (2011), Giersiepen et al. (1990), Heuser and Opitz (1980) as regards the hemolysis parameters. While this discrepancy can be significant on the predictive quality of the computational model itself, it can also lead to unfavorable results when optimization is considered. To avoid additional cumbersome and often unfeasible experiments, this work proposes to approximate these parameters as uncertain variables. To this extent, we consider

$$\boldsymbol{\omega}^h = (C, \alpha, \beta) \quad \text{and} \quad \boldsymbol{\omega}^\mu = (\lambda, n, \mu_0, \mu_\infty), \tag{8}$$

as two independent M–dimensional vectors of uncertain variables, with $M = 3$ and $M = 4$ for the case of hemolysis and non-Newtonian parameters, respectively. Each uncertain variable is associated with a probability density function resulting in corresponding vectors of mean values and standard deviations, denoted as $\bar{\boldsymbol{\omega}}^h, \bar{\boldsymbol{\omega}}^\mu$ and $\boldsymbol{\sigma}^h, \boldsymbol{\sigma}^\mu$, respectively. For the sake of brevity, the superscript of the previously defined vectors is dropped in what follows and only specified when necessary.

Since the primal problem is now dependent on a number of uncertain variables, so is the QoI, i.e., $F(\boldsymbol{\omega})$. We consider the propagation of the uncertainties to the QoI based on the FOSM method, which develops the QoI based on a truncated first-order Taylor series expansion around the mean values of the uncertain variables, viz.

$$F(\boldsymbol{\omega}) = F(\bar{\boldsymbol{\omega}} + \boldsymbol{\delta\omega}) \approx F(\bar{\boldsymbol{\omega}}) + \left.\frac{dF}{d\boldsymbol{\omega}}\right|_{\bar{\boldsymbol{\omega}}} \cdot \boldsymbol{\delta\omega}. \tag{9}$$

Assuming that the covariance matrix of the uncertain variables is diagonal, it can be shown based on expression (9) that the first two statistical moments of the QoI can be approximated as

$$\mu_F = F(\bar{\boldsymbol{\omega}}) \quad \text{(mean)} \tag{10}$$

$$\sigma_F^2 = \left[\frac{dF}{d\omega_i}\right]_{\bar{\boldsymbol{\omega}}}^2 \sigma_i^2 \quad \text{(variance)} \tag{11}$$

see, e.g., (Kriegesmann and Lüdeker 2019). Based on FOSM, the mean of the QoI can be approximated by one computation at $\boldsymbol{\omega} = \bar{\boldsymbol{\omega}}$, while the variance requires in addition the derivatives of the QoI w.r.t. the uncertain variables for $\boldsymbol{\omega} = \bar{\boldsymbol{\omega}}$. Note, however, that the estimation of both statistical moments is independent of the underlying probability density function of the uncertain variables and only requires the mean value and variance (standard deviation) vectors to be chosen by the user.

In comparison to other UQ methods, e.g., based on Monte Carlo techniques, the FOSM method allows the evaluation of the sought statistical moments of the QoI and their derivatives at a reasonable number of primal/adjoint evaluations per shape update, as illustrated in Sect. 2.3.4. Furthermore, it decouples the optimization process from the requirement of specifying a probability density function, which can be ambiguous because of insufficient relevant experimental data due to the nature of the problem. Higher-order methods of moments, e.g., the second-order second-moment (SOSM) method (Papoutsis-Kiachagias et al. 2012), increase the necessary computations, because higher-order derivatives need to be evaluated. The FOSM method avoids this and is by construction sufficiently accurate when the QoI is approximately linear in a neighborhood close to the selected mean value of the uncertain variables. To this end, we present a sensitivity analysis study w.r.t. the uncertain variables in "Appendix C".

This work considers a low number of uncertain variables and is therefore computationally reasonable to approximate the derivatives of Eq. (11) based on the finite differences method, viz.

$$\frac{dF}{d\omega_i}(\bar{\boldsymbol{\omega}}) \approx \frac{F(\bar{\omega}_1, \dots, \bar{\omega}_i + \epsilon, \dots, \bar{\omega}_M) - F(\bar{\omega}_1, \dots, \bar{\omega}_i, \dots, \bar{\omega}_M)}{\epsilon}. \tag{12}$$

Note that only a first-order accurate finite differences scheme is considered, since a similar first-order assumption is already made in the construction of the method, cf. Eq. (9). The determination of Eq. (12) requires M additional simulations. However, it is worth noting that in the case of uncertain hemolysis parameters, the determination of the QoI does not require the recomputation of the flow field but only the computation of the hemolysis equation due to the one-way coupling assumed between the flow and the hemolysis equation. The numerical solution of the latter is significantly faster than the solution of the flow field and therefore the cost of computing Eq. (12) can be considered negligible. For the uncertain non-Newtonian parameters, even though the flow field needs to be recomputed to estimate the perturbed QoI, the numerical method can be warm-started from the flow field of the unperturbed state, since the topology of the computational mesh is the same. Therefore, in both cases, the computational cost of the M additional simulations required for the estimation of Eq. (12) is significantly smaller than M CFD solutions.

2.3 Robust shape optimization problem

Let $F(\boldsymbol{y}, \boldsymbol{u}) \in \mathbb{R}$ denote an objective functional that depends exclusively on a state $\boldsymbol{y} \in Y$ and a control $\boldsymbol{u} \in U$, where Y, U denote the Banach spaces of state and control, respectively. We assume that the state is unique on $\boldsymbol{u}$ and thus the control to state mapping $\boldsymbol{u} \mapsto \boldsymbol{y}(\boldsymbol{u})$ exists. Therefore, one can consider a reduced objective functional $F(\boldsymbol{y}(\boldsymbol{u}), \boldsymbol{u}) =: \hat{F}(\boldsymbol{u})$. Practically, the above statements mean that given a specific control $\boldsymbol{u}^* \in U$, the objective functional $\hat{F}(\boldsymbol{u}^*)$ is determined through the, now hidden, solution of the state equations. The goal of a deterministic optimization problem is to minimize the (reduced) objective functional by updating the control until $\boldsymbol{u}^*$ is sufficiently approximated, for which $\hat{F}(\boldsymbol{u}^*) \le \hat{F}(\boldsymbol{u}^+)$, $\forall \boldsymbol{u}^+ \in \mathcal{N}$, where $\mathcal{N}$ denotes a neighborhood of $\boldsymbol{u}^*$.

Consider now that the state, initially assumed to depend only on the control and the underlying physics (state equations), is unpredictably perturbed due to reasons unrelated to the control, e.g., due to an inconsistent/simplified modeling of the physics resulting to a false estimation of the state. The solution $\boldsymbol{u}^*$ found by the deterministic problem is likely not to be optimal anymore. The resolution of this discrepancy is addressed by robust optimization, in which a certain level of uncertainty is prescribed to select modeling parameters. The goal of robust optimization is not to arrive at a set of optimal solutions for each probable state but rather to arrive at a control that likely performs better than the initial for each probable state, that is expressed by the mean of the QoI. At the same time, the optimization should target at a shape that exhibits minimum variations on its performance w.r.t. the uncertain input, which is expressed by the standard deviation of the QoI. To this end, the objective functional is considered as a statistical quantity. The optimization targets the minimization of its statistical moments rather than its value at each probable state, viz.

$$J = W_1 \mu_F + W_2 \sigma_F, \tag{13}$$

where μ_F and σ_F correspond to the mean value and standard deviation of a QoI, respectively, and W_1, W_2 denote weights to be chosen before the optimization starts.

In this paper, we consider the control $\boldsymbol{u}$ to be associated with the shape Γ_{w} of our geometry and to be of deterministic nature, i.e., not subject to uncertainties. Therefore, one can express the objective functional as $J(\boldsymbol{y}(\boldsymbol{u}, \boldsymbol{\omega}), \boldsymbol{u})$, where in accordance to Sect. 2.2, $\boldsymbol{\omega}$ stands for an uncertain variable vector that implicitly acts on the objective functional (13) through its influence on the state. We are interested in optimizing the shape based on a gradient-based method and we therefore require

$$\frac{dJ}{d\boldsymbol{u}} = W_1 \frac{d\mu_F}{d\boldsymbol{u}} + W_2 \frac{d\sigma_F}{d\boldsymbol{u}}, \tag{14}$$

which based on the UQ approach followed herein [see Eqs. (10, 11)] can be expanded as

$$\frac{dJ}{d\boldsymbol{u}} = W_1 \frac{dF}{d\boldsymbol{u}}(\bar{\boldsymbol{\omega}}) + W_2 \frac{1}{\sigma_F} \left(\frac{d^2F}{d\omega_i \boldsymbol{u}} \Big|_{\bar{\boldsymbol{\omega}}} \lambda_i \right), \tag{15}$$

where the vector $\boldsymbol{\lambda} \in \mathbb{R}^M$ is defined as

$$\boldsymbol{\lambda} = \left(\frac{dF}{d\omega_1} \Big|_{\bar{\boldsymbol{\omega}}} \sigma_1^2, \frac{dF}{d\omega_2} \Big|_{\bar{\boldsymbol{\omega}}} \sigma_2^2, \dots, \frac{dF}{d\omega_M} \Big|_{\bar{\boldsymbol{\omega}}} \sigma_M^2 \right). \tag{16}$$

The determination of Eq. (15) requires the computation of $dF/d\boldsymbol{\omega}$, $dF/d\boldsymbol{u}$ and $d^2F/d\boldsymbol{\omega}d\boldsymbol{u}$ at $\boldsymbol{\omega} = \bar{\boldsymbol{\omega}}$. The computation of the derivatives w.r.t. the uncertain variables is addressed in Sect. 2.2.

2.3.1 Determination of first-order derivative w.r.t. the control

We are interested in applying a parameter-free shape optimization method, which means that instead of controlling the shape through a finite number of parameters, e.g., control points of B-splines (Farhikhteh et al. 2023), the complete shape or rather the discrete representation of the shape is considered as the control. To this extent, the number of control variables can be in the order of $\mathcal{O}(10^5)$ and derivative computation methods that scale with the number of control variables, e.g., finite differences, are unfeasible.

Therefore, the continuous adjoint method is employed for the determination of the sought first-order derivative w.r.t. the control. The adjoint (dual) to the primal problem described in Sect. 2.1 reads

$$\hat{R}^p = -\frac{\partial \hat{v}_i}{\partial x_i} = 0 \tag{17}$$

$$\begin{aligned} \hat{R}_i^v = {} & \hat{v}_j \rho \frac{\partial v_j}{\partial x_i} - v_j \rho \frac{\partial \hat{v}_i}{\partial x_j} - \frac{\partial}{\partial x_j} \left(2\tilde{\mu}\hat{S}_{ij} - \hat{p}\delta_{ij} - \hat{\mu}X_{ij} - \hat{h}B_{ij} \right) \\ & - H_L \frac{\partial \hat{h}}{\partial x_i} = 0 \end{aligned} \tag{18}$$

$$\hat{R}^H = v_j \frac{\partial \hat{h}}{\partial x_j} - C^{\frac{1}{\beta}} \bar{\tau}^{\frac{\alpha}{\beta}} \hat{h} = 0 \tag{19}$$

$$\begin{aligned} & \hat{R}^\mu = (\hat{\mu} - \Lambda) + 2S_{ij} \frac{\partial \hat{v}_i}{\partial x_j} = 0, \\ & \qquad \text{with} \quad \Lambda = 2\hat{h} \frac{\alpha}{\beta} \tilde{\mu} C^{\frac{1}{\beta}} \left(1 - H_L\right) \bar{\tau}^{\left(\frac{\alpha}{\beta} - 2\right)} S_{ij} S_{ij}. \end{aligned} \tag{20}$$

Adjoint velocity components and pressure are denoted by $\hat{v}_i$ and $\hat{p}$, respectively. Adjoint hemolysis is denoted by $\hat{h}$ and adjoint viscosity is denoted by $\hat{\mu}$, while $\hat{S}_{ij} = 0.5\left(\partial\hat{v}_i/\partial x_j + \partial\hat{v}_j/\partial x_i\right)$ stands for the adjoint strain-rate tensor components. Tensors B_{ij} and X_{ij} relate to the primal hemolysis and non-Newtonian models, respectively, and for the specific models employed in this work can be computed based on

$$\begin{aligned} & B_{ij} = 2C^{\frac{1}{\beta}} \left(1 - H_L\right) \tilde{\mu}^2 \frac{\alpha}{\beta} \bar{\tau}^{\left(\frac{\alpha}{\beta} - 2\right)} S_{ij} \quad \text{and} \\ & X_{ij} = 2(n-1)(\mu_0 - \mu_\infty)\left(1 + (\lambda\dot{\gamma})^2\right)^{\frac{n-3}{2}} \lambda^2 S_{ij}. \end{aligned} \tag{21}$$

The boundary conditions employed to close the adjoint field equations are as follows:

- Zero Dirichlet adjoint velocity and zero Neumann adjoint pressure and adjoint hemolysis on Γ_{in} and Γ_{w},
- Dirichlet adjoint pressure, adjoint hemolysis, and adjoint tangential velocity components based on

$$\hat{p} = \rho \hat{v}_n v_n + \tilde{\mu} \frac{\partial \hat{v}_n}{\partial n} + \rho H_L^\beta (1 - \beta) \qquad \text{on} \quad \Gamma_{\mathrm{out}} \tag{22}$$

$$\hat{h} = -\rho\beta H_L^{\beta-1} \qquad \text{on} \quad \Gamma_{\text{out}} \tag{23}$$

$$\hat{v}_i^t = 0 \qquad \text{on} \quad \Gamma_{\text{out}}, \tag{24}$$

where a superscript t implies the tangential components of a vector and a subscript n implies the normal to the surface component of a vector, i.e., $v_n = v_i n_i$ with n_i denoting the normal vector. The normal component of adjoint velocity is approximated by satisfying adjoint continuity, Eq. (17), on the outlet.

The resulting system of field adjoint Eqs. (17-20) and their corresponding boundary conditions is derived by extension of the derivations presented in Bletsos et al. (2023, 2021) to consider cross-coupling terms between primal hemolysis and non-Newtonian viscosity equations. Key aspects of the derivation process of the employed adjoint system can be found in "Appendix B". Note that in the FOSM approach, the sought derivative must be computed at the mean values of the uncertain variables. Therefore, in the context of uncertain hemolysis or non-Newtonian parameters, the computation of the primal and adjoint systems is realized for $\boldsymbol{\omega} = \bar{\boldsymbol{\omega}}^{\boldsymbol{h}}$ or $\boldsymbol{\omega} = \bar{\boldsymbol{\omega}}^{\boldsymbol{\mu}}$, respectively.

Once the primal and adjoint equation systems are solved, the sought derivative can be computed based on

$$\frac{dF}{d\boldsymbol{u}} = -\left(\tilde{\mu}\frac{\partial \hat{v}_i}{\partial n} - \hat{h}B_{ij}n_j - \hat{\mu}X_{ij}n_j\right)\frac{\partial v_i}{\partial n}\boldsymbol{\Delta\Gamma} \qquad \text{on} \quad \Gamma_{\text{w}}, \tag{25}$$

where $\boldsymbol{\Delta\Gamma}$ denotes the vector of face areas of the discretized wall boundary.

Similar to the primal state equations, the numerical solution of their adjoint counterparts is based on the finite volume method employed by *FreSCo*$^+$. It is interesting to note that similar to its primal counterpart, the adjoint hemolysis equation (19) is again one-way coupled to the adjoint flow equations (17,18), but this time the coupling direction is reversed. This implies that adjoint hemolysis is required for the solution of the adjoint flow equations with no retroaction to it. From a numerical point of view, this allows us to independently solve the adjoint hemolysis equation based solely on information from the primal solution. Tensors B_{ij} and X_{ij} require only primal flow information and can thus be computed once, before the solution of any adjoint equation. The adjoint pressure–velocity coupling is resolved by a similar to the primal SIMPLE algorithm. Note that in adjoint systems, the information transfer is reversed w.r.t. to the primal. To this end, the convective terms are discretized by the downwind analogy of QUICK. The diffusive term is self-adjoint, and thus, the same discretization schemes as in the primal can be employed. The remaining terms in adjoint momentum, stemming from hemolysis and non-Newtonian properties, are treated as source terms. Similar to its primal counterpart, adjoint viscosity is computed by means of an explicit approach where the adjoint velocity components of the previous adjoint pressure–velocity coupling iteration are employed in Eq. (20). Due to the algebraic nature of the adjoint viscosity equation, no boundary conditions are required. When adjoint viscosity is required on a boundary face, its value is extrapolated from the adjacent cell center.

2.3.2 Determination of second-order mixed derivative

The computation of Eq. (15) requires the estimation of the mixed second-order derivative of the QoI w.r.t the control and the uncertain variables. While the computation of second-order derivatives can in general be a cumbersome task, Eq. (15) does not require the explicit computation of the mixed second derivative but instead its projection on the $\boldsymbol{\lambda}$ vector, as noted by Fragkos et al. (2019) and Krüger et al. (2023). This alleviates some of the computational effort, since the projection can be efficiently computed based on an additional adjoint system, as suggested by Fragkos et al. (2019), or by an efficient finite differences method, as suggested by Krüger et al. (2023). The finite differences approach is followed herein. The interested reader is pointed to the original paper for further details.

The sought projected derivative can be computed to second-order accuracy based on

$$\frac{d^2F}{d\boldsymbol{u}d\omega_i}\lambda_i \approx \frac{1}{2\,\epsilon^*}\left[\frac{dF}{d\boldsymbol{u}}(\bar{\omega}_i + \epsilon^*\lambda_i) - \frac{dF}{d\boldsymbol{u}}(\bar{\omega}_i - \epsilon^*\lambda_i)\right]. \tag{26}$$

The essential difference between expression (26) and a classic finite differences method is that while the latter needs to perturb each individual uncertain variable while keeping the rest constant, the former can approximate the sought quantity by perturbing the complete vector of mean values simultaneously. Therefore, instead of the $4M$ additional simulations that would otherwise be required for the approximation of the second-order mixed derivative, the projected quantity can be approximated to second-order accuracy with 4 additional simulations, i.e., 2 primal and 2 adjoint simulations at $(\bar{\omega}_i + \epsilon^*\lambda_i)$ and $(\bar{\omega}_i - \epsilon^*\lambda_i)$. The value of the perturbation size is $\epsilon^* = \hat{\epsilon}/\|\lambda\|$, where $\hat{\epsilon}$ is fixed as the authors of the original publication suggest.

2.3.3 Determination of descent direction

In parameter-free shape optimization, the computation of the shape sensitivity, i.e., Eq. (15), is not sufficient to optimize the shape. An in-depth mathematical explanation of this restriction can be found in Allaire et al. (2021). In practice, we are interested to update the shape and the corresponding mesh of the domain without the need of re-meshing. To this extent, we are searching for a deformation field that can sustain, as much as possible, the quality of the mesh, so that the optimization process can continue uninterrupted. Therefore, a descent direction (deformation) field over the design surface is sought and it must be sufficiently smooth, so that each shape update results in feasible solutions in which one can numerically solve the primal and adjoint equations. This topic is extensively discussed in the recent publication Radtke et al. (2023).

A variety of methods exists to identify such a descent direction. A gross classification can be made depending on the number of additional steps required after the approximation of the shape sensitivity. On the one hand, methods such as sensitivity filtering (Kröger and Rung 2015) or the, frequently called, Laplace–Beltrami method (Vassberg and Jameson 2006), compute a deformation field on the shape of the domain. Subsequently, another step needs to be taken to propagate the field to the interior nodes. On the other hand, methods like the Steklov–Poincaré (Welker 2016) or the p-Laplace (Müller et al. 2021) are able to compute the deformation field in the complete computational domain in one step. Based on this and since the p-Laplace method requires a much larger computational effort due to its highly non-linear character, this paper employs the Steklov–Poincaré method.

The descent direction field is thus computed based on

$$\frac{\partial}{\partial x_k}\left(\mu^{\mathrm{SP}}\frac{\partial d_j}{\partial x_k}\right) = 0 \qquad \text{in} \quad \Omega \tag{27}$$

$$\mu^{\mathrm{SP}}\frac{\partial d_j}{\partial x_k}n_k = sn_j \qquad \text{on} \quad \Gamma_{\mathrm{w}}, \tag{28}$$

where μ^{SP} corresponds to a diffusivity coefficient. Herein, it is set to the reciprocal of the distance from the nearest wall boundary. The quantity s refers to the local shape sensitivity of the discretized shape and corresponds to dJ/du for a boundary face on Γ_{w}. The solution of Eq. (27) is realized via the finite volume discretization for a diffusive term and the field d_j is computed on the cell centers. The mesh update is then realized by a Shepard's interpolation (Shepard 1968) of the cell-centered descent direction to the nodal positions of the mesh. Schematically, this is illustrated for a node by $\tilde{\boldsymbol{d}} = \mathrm{INT}(\boldsymbol{d})$ and it implies the inverse distance weighting interpolation strategy from all cells in which the node exists. Once the nodal deformations are available, the mesh can be updated based on

$$\tilde{\boldsymbol{x}}^{i+1} = \tilde{\boldsymbol{x}}^{i} - \alpha\tilde{\boldsymbol{d}}^{i}, \tag{29}$$

for all nodes of the mesh. Here, $\tilde{\boldsymbol{x}}$ denotes the position vector of a node, α denotes a constant step size, and the superscript i denotes the optimization iteration index.

2.3.4 Optimization algorithm

The adjoint-assisted optimization algorithm for the FOSM-based robust shape optimization problem is presented in Algorithm 1. Initially, the uncertain variables are set to their mean values and the primal problem is solved (line 2). Then, a primal problem is simulated for each uncertain variable, in which it is perturbed, while the remaining are fixed to the mean values (line 4). Based on these simulations, the mean value and standard deviation of the QoI can be calculated. The algorithm then checks for convergence by comparing the relative change of the objective from one step to the other (line 7). If convergence is not achieved, an adjoint problem is solved for uncertain variables set to their mean values (line 10). For the determination of the second-order mixed derivative, all uncertain variables are simultaneously perturbed by $\pm\epsilon^{*}\lambda$ and the corresponding primal and adjoint problems are solved (lines 12,13). The sensitivity is then calculated (line 15) and passed as input to the descent direction computation (line 16). Once this is computed, each numerical node is updated (line 17) and the optimization continues to the next step.

Algorithm 1 FOSM-based robust parameter-free shape optimization algorithm using the adjoint method.

```
Require: initial shape $\boldsymbol{u}^0 \equiv \Gamma_\mathrm{w}^0$, $\bar{\boldsymbol{\omega}}$, $\boldsymbol{\sigma}$, $\hat{\epsilon} > 0$, $\epsilon_k > 0$, $\epsilon^\mathrm{conv} > 0$, $\alpha > 0$, $1 \geq W_1, W_2 \geq 0$
1:  for $i = 0, 1, \ldots$ do
2:      Compute the primal problem at $(\bar{\boldsymbol{\omega}}, \boldsymbol{u}^i)$ to find $\mu_F$ (Eq. (10)).
3:      for $k = 1, \ldots, M$ do
4:          Compute the primal problem at $(\bar{\omega}_k + \epsilon_k, \boldsymbol{u}^i)$ to find $\frac{dF}{d\omega_k}(\bar{\boldsymbol{\omega}}) \rightarrow \lambda_k$ (Eqs. (12, 16)).
5:      end for
6:      Calculate $\sigma_F = \sqrt{\sigma_F^2} \rightarrow J(\boldsymbol{u}^i)$ (Eqs. (11, 13)) .
7:      if $\left(|J(\boldsymbol{u}^i) - J(\boldsymbol{u}^{i-1})|/J(\boldsymbol{u}^{i-1})\right) \cdot 100 \leq \epsilon^\mathrm{conv}$ then
8:          break
9:      end if
10:     Compute the adjoint problem at $(\bar{\boldsymbol{\omega}}, \boldsymbol{u}^i)$ to find $\frac{dF}{d\boldsymbol{u}}$ (Eq. (25)).
11:     Calculate $\epsilon^* = \hat{\epsilon}/\|\boldsymbol{\lambda}\|$.
12:     Compute the primal problem at $(\bar{\boldsymbol{\omega}} \pm \epsilon^* \boldsymbol{\lambda}, \boldsymbol{u}^i)$.
13:     Compute the adjoint problem at $(\bar{\boldsymbol{\omega}} \pm \epsilon^* \boldsymbol{\lambda}, \boldsymbol{u}^i)$ to find $\frac{dF}{d\boldsymbol{u}}(\bar{\boldsymbol{\omega}} \pm \epsilon^* \boldsymbol{\lambda}, \boldsymbol{u}^i)$ (Eq. (25)).
14:     Calculate the projected mixed derivative $\frac{d^2F}{d\boldsymbol{u}d\omega_k}\lambda_k$ (Eq. (26)).
15:     Calculate the shape sensitivity $\frac{dJ}{d\boldsymbol{u}}$ (Eq. (15)).
16:     Compute the descent direction field $\boldsymbol{d}^i$ (Eqs. (27, 28)) and interpolate cell values to nodes, $\tilde{\boldsymbol{d}}^i = \mathrm{INT}(\boldsymbol{d}^i)$.
17:     Update shape (Eq. (29)).
18: end for
```

Note that the presented algorithm distinguishes between statements with the keyword "Compute" and "Calculate". The former can require substantial computational resources, since it relates to primal or adjoint CFD simulations or the computation of the descent direction, while the latter requires trivial resources for the determination of the sought quantities. Furthermore, it is worth noting that the computations in line 4 can be trivially parallelized, since they are independent of each other. The same holds for the primal simulations in line 12 and the subsequent corresponding adjoint simulations in line 13. Overall, one shape update requires $6 + M$ CFD simulations. However, it must be noted that in addition to the trivial parallelization possibility in several stages of the algorithm, the cost of the M simulations related to the loop in lines 3–5 is significantly lower to the cost of full CFD simulations. The finite differences conducted therein require only the perturbation of the mean uncertain variables. Therefore, in the case of uncertain hemolysis parameters and due to the one-way coupling of the hemolysis model with the flow equations, the main flow solution, which is already available from line 2 of the algorithm, can be used to arrive with trivial resources in the sought derivative. In the case of uncertain non-Newtonian parameters, the flow equations need to be recomputed; however, the simulation can be warm-started from the solution of the unperturbed flow, thus resulting in a significant speed-up of the M additional simulations. To highlight this, we present Fig. 1, which shows the wall clock time for the first (initial shape) primal simulation and for the computations in lines 3–5 of the algorithm. The results shown therein refer to the case studied in Sect. 3. All computations are parallelized using 90 CPUs.

Note that in the case of uncertain hemolysis parameters, the wall clock time of the computations in lines 3–5 are significantly faster, since the primal flow is already resolved and due to the one-way coupling, as outlined above. In addition, all perturbed primal simulations can be performed in parallel. This would make the computational cost of the loop in lines 3–5 approximately equal to the cost of the slowest simulation, e.g., based on Fig. 1, 21.37 s and 174.07 s for the uncertain hemolysis parameters and non-Newtonian parameters, respectively.

3 Applications

The 3D geometry studied in this paper refers to an idealized arterial bypass graft. An arterial bypass graft is a segment of a healthy (biological or artificial) blood vessel that is used to divert blood around narrowed or occluded parts of an impaired artery. A sketch of the initial geometry is shown in Fig. 2. The diameters of the bypass graft and the artery are set to $D^{\mathrm{graft}} = 14\,\mathrm{mm}$ and $D^{\mathrm{artery}} = 9\,\mathrm{mm}$, respectively. The size of the idealized impaired artery geometry is chosen, so that it approximately matches a common iliac or femoral artery (Wazzan et al. 2022).

An extensive FSI and CFD qualitative study was performed on this geometry in Bletsos et al. (2024). Therein, it was identified that the shape of the anastomosis, i.e., the connection between the implant and the impaired artery, is one of the most critical parameters in which one can intervene for the hemodynamic response of the implant. Based on this finding and considering its clinical relevance, this paper is motivated to formally optimize the shape, i.e., in contrast to the parametric study conducted in Bletsos et al. (2024), based on the methodology presented in Sect. 2.

3.1 Primal simulation setup

The reproducible process for the discretization of the computational domain is thoroughly described in Bletsos et al. (2024) and results in a block-structured mesh of 315k control volumes. The $\Gamma_{\mathrm{w}}^{\mathrm{up}}$ boundary patch is considered as a wall boundary, thus mimicking a complete occlusion of the impaired artery.

The shape optimization problem considers steady-state flow conditions. However, the steady inflow is chosen based on the peak volume flux of a suitably scaled flow pulse for a patient in rest conditions (Wilson et al. 2005). The choice of performing the optimization at the peak volume flux is made based on the anticipation of maximum hemolysis induction potential at this condition. The flux is then redistributed along the inlet based on a Poiseuille velocity profile, as shown in Fig. 3.

The prescribed flux is $Q^{\mathrm{in}} \approx 18\,\mathrm{ml/s}$ and amounts to a Reynolds number of

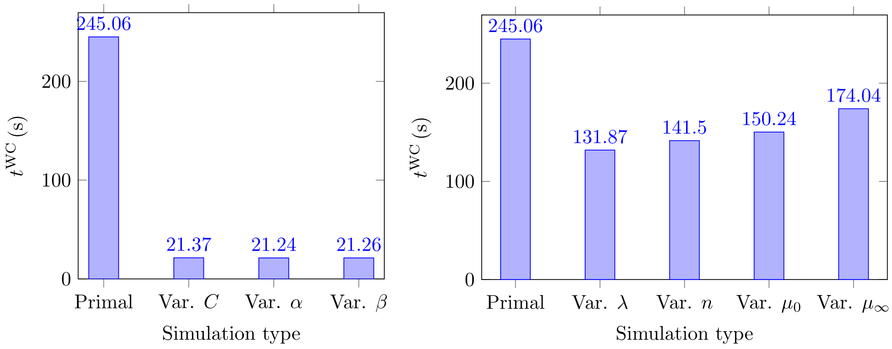

Fig. 1 Idealized arterial bypass graft (Sect. 3): wall clock time required for primal problem solution and perturbed primal problem, lines 2 and 4 (Algorithm 1), respectively. Left: uncertain hemolysis parameters Right: uncertain non-Newtonian parameters

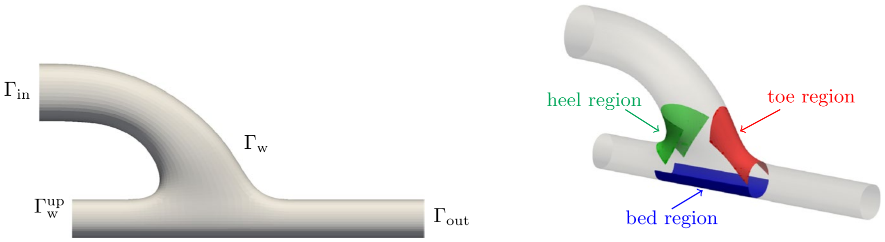

Fig. 2 Sketch of the initial idealized geometry of the arterial bypass graft. Left: side view of the geometry annotated with the boundary patches. Right: perspective view of the geometry annotated with the critical regions of the anastomosis

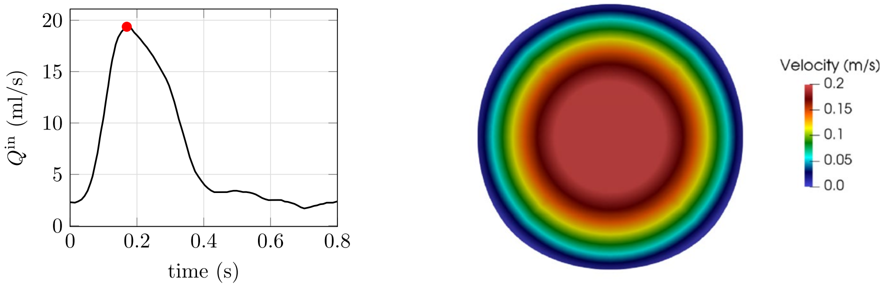

Fig. 3 Left: volume flux for rest conditions marked by a red point at the time instant in which the steady-state optimization studies are performed. Right: velocity profile at the inlet based on the prescribed volume flux

$$\mathrm{Re} = \frac{\rho\, v^{\mathrm{in}}\, D^{\mathrm{graft}}}{\mu^{\mathrm{N}}} \approx 455 \quad \text{with} \quad v^{\mathrm{in}} = \frac{4\, Q^{\mathrm{in}}}{\pi (D^{\mathrm{graft}})^2} \tag{30}$$

and $\mu^{\mathrm{N}} = 3.5\,\mathrm{mPa}\cdot\mathrm{s}$ denoting the Newtonian viscosity of blood in high shear rates. Based on the prescribed flow conditions, an average dimensionless near-wall spacing from the walls is estimated at $y^+ \approx \mathcal{O}(10^{-2})$. Furthermore and due to the employed rigid wall assumption, a zero pressure is prescribed at the outlet of the computational domain. The fluid is modeled as non-Newtonian and the viscosity computation is based on the Carreau model, cf. Eq. (4).

3.2 Optimization setup

The optimization studies consider the complete Γ_{w} boundary section to be subjected for design, while $\Gamma_{\mathrm{w}}^{\mathrm{up}}$ is bound to its initial configuration. Furthermore and as discussed in Sect. 2, the hemolysis or non-Newtonian parameters are considered to be uncertain. To this end, each uncertain variable is associated with a mean value and a standard deviation.

3.2.1 Uncertain hemolysis parameters

In this case, the non-Newtonian parameters are fixed to the Carreau parameters, i.e., $\lambda = 3.313\,\mathrm{s}$, $n = 0.357\,[-]$, $\mu_0 = 56\,\mathrm{mPa}\cdot\mathrm{s}$, $\mu_\infty = 3.5\,\mathrm{mPa}\cdot\mathrm{s}$. The vector of uncertain parameters is then defined as

$$\boldsymbol{\omega} = \boldsymbol{\omega}^{\boldsymbol{h}} = (C, \alpha, \beta). \tag{31}$$

The hemolysis parameters appearing in Eq. (5), which are deduced from data-fitting experimental results from fully controlled configurations, see, e.g., Giersiepen et al. (1990), are here considered uncertain. The mean value and standard deviation vectors are prescribed as

$$\begin{aligned} \bar{\boldsymbol{\omega}} &= \bar{\boldsymbol{\omega}}^{\boldsymbol{h}} = (3.6 \cdot 10^{-7}, 2.416, 0.785) \quad \text{and} \\ \boldsymbol{\sigma} &= \boldsymbol{\sigma}^{\boldsymbol{h}} = (1.08 \cdot 10^{-7}, 0.4832, 0.0707). \end{aligned} \tag{32}$$

The choice of $\bar{\boldsymbol{\omega}}^{\boldsymbol{h}}$ is made based on the frequency that this set of parameters is used in computational studies in literature; see, e.g., Yu et al. (2017), Thamsen et al. (2015). We note that this choice is ambiguous and, therefore, the results presented in this study are discussed in a qualitative manner rather than quantitative. The standard deviations are selected under the assumption of a normal distribution, such that parameter sets proposed in the literature fall within approximately $\pm 2\sigma$. This corresponds to a 95.4% confidence interval, reflecting the belief that these values represent typical variability. Additionally, the prescribed mean and standard deviation vectors assure that the probable space $[-3\sigma, 3\sigma]$ (99.73 % probability for a normal distribution) does not include non-physical solutions such as $\beta > 1$.

3.2.2 Uncertain non-Newtonian parameters

In this case, the hemolysis parameters are fixed to the set of parameters employed as $\bar{\boldsymbol{\omega}}^{\boldsymbol{h}}$ in Eq. (32). The vector of uncertain variables is defined as

$$\boldsymbol{\omega} = \boldsymbol{\omega}^{\boldsymbol{\mu}} = (\lambda, n, \mu_0, \mu_\infty). \tag{33}$$

In this case, the parameters employed to model the non-Newtonian viscosity of blood in Eq. (4) are considered uncertain. These parameters are, similarly to the hemolysis parameters, deduced by fitting experimental data. The mean value and standard deviation vectors are prescribed as

$$\begin{aligned} \bar{\boldsymbol{\omega}} &= \bar{\boldsymbol{\omega}}^{\boldsymbol{\mu}} = (3.313, 0.357, 56, 3.5) \quad \text{and} \\ \boldsymbol{\sigma} &= \boldsymbol{\sigma}^{\boldsymbol{\mu}} = (0.497, 0.0714, 14, 0.07). \end{aligned} \tag{34}$$

Based on the employed mean and standard deviation vectors and by assuming underlying normal distributions for each uncertain variable, Fig. 4 shows the probable (within 95.4% of each uncertain variable probability) space in which viscosity could be represented.

As shown, the choice of $\bar{\boldsymbol{\omega}}$ and $\boldsymbol{\sigma}$ does not allow for non-physical solutions, e.g., negative viscosities, and sustains necessary characteristics of a blood non-Newtonian model, such as converging to an experimentally measured constant viscosity at high shear rates.

3.2.3 General optimization parameters

For both cases of uncertain modeling parameters, optimization studies are performed for different sets of weighting parameters (W_1, W_2), cf. Eq. (13). Specifically, optimizations are performed for

- $(W_1, W_2) = (1, 0)$ denoted as "DET",
- $(W_1, W_2) = (0.5, 0.5)$ denoted as "MIXED",
- $(W_1, W_2) = (0, 1)$ denoted as "STD".

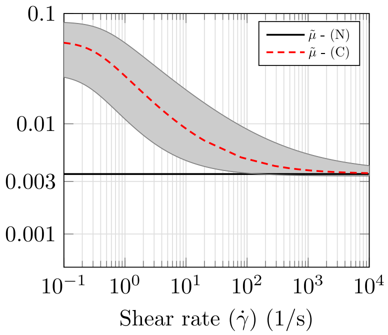

Fig. 4 Newtonian (N) and non-Newtonian viscosity (C), based on the Carreau model. Gray area denotes the range in which viscosity is most likely (95.4% probability) to be represented based on the employed $\bar{\boldsymbol{\omega}}$ and $\boldsymbol{\sigma}$

Note that based on our setup, the DET optimization is identical for both uncertain hemolysis and uncertain non-Newtonian parameters.

Additionally, the perturbation size ϵ employed in the finite differences computation of the first-order derivative of the QoI w.r.t. the uncertain variables (Eq. (12)) is set to approximately three orders of magnitude smaller than each mean value of the perturbed uncertain variable. The dynamically changing perturbation size for the projected second-order mixed derivative is computed based on $\hat{\epsilon} = 10^{-5}$. Convergence is monitored by $\epsilon^{\text{conv}} = 0.001$. We note that this corresponds to a very strict convergence criterion but might allow us to explore additional shapes in the optimization sequence. Usual choices would refer to $\epsilon^{\text{conv}} = 0.1$; see, e.g., Radtke et al. (2023). However, due to the increased computational cost of a robust shape optimization method in comparison to a deterministic one, we also apply as a stop condition the maximum number of optimization iterations, which for the study at hand is set to 230, based on our computational capabilities. The fixed optimization step size is implicitly determined on the first optimization iteration by a maximum displacement approach, that is

$$\alpha = \frac{D^{\text{graft}}}{140}\left(\max_{\boldsymbol{x}\in\Gamma_{\text{w}}}\left(\|\boldsymbol{d}(\boldsymbol{x})\|_2\right)\right)^{-1}, \tag{35}$$

which scales the descent direction computed by Eqs. (27, 28), so that the maximum applied deformation on the first optimization iteration is equal to $D^{\text{graft}}/140$.

The QoI F, the statistical moments of which we want to minimize, is the hemolysis index defined in Eq. (7).

3.3 Results

The results are presented for each set of uncertain variables separately. A discussion is then included on the collective results of the optimization studies. Selected designs are then subsequently evaluated by FSI simulations.

3.3.1 Uncertain hemolysis parameters

Figure 5 shows the FOSM-estimated decrease of the mean value and standard deviation of the QoI for the three optimization cases with uncertain hemolysis parameters. As shown therein, all cases manage to minimize the mean by more than 35%, even though the STD case does not explicitly involve the optimization of the mean in the formulation of the problem. As expected, the DET case leads to the highest estimated decrease of approximately 52%. Specifically for the DET case, the mean value of the QoI is decreased from $7.00 \cdot 10^{-8}$ to $3.37 \cdot 10^{-8}$ and the standard deviation from $2.24 \cdot 10^{-8}$ to $1.21 \cdot 10^{-8}$. Furthermore, we present in Fig. 6 the relative change of the objective functional in percent for two subsequent shapes in the optimization history. As shown there, all methods manage to arrive at a relative change smaller that 0.2%, which is, however, significantly larger than the employed $\epsilon^{\text{conv}} = 0.001\%$ threshold. This convergence can be accelerated by an increase of the employed step size. Interestingly, the DET optimization case outperforms the other two in the decrease of the standard deviation as well, even though it does not explicitly account for its minimization. This result indicates an inherent robustness of the

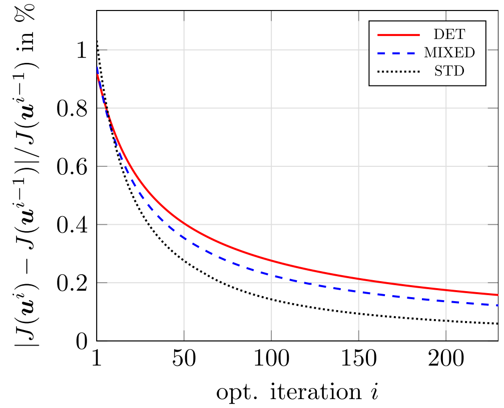

Fig. 6 Optimizations for uncertain hemolysis parameters. Relative change of the objective functional in percent for two subsequent shapes

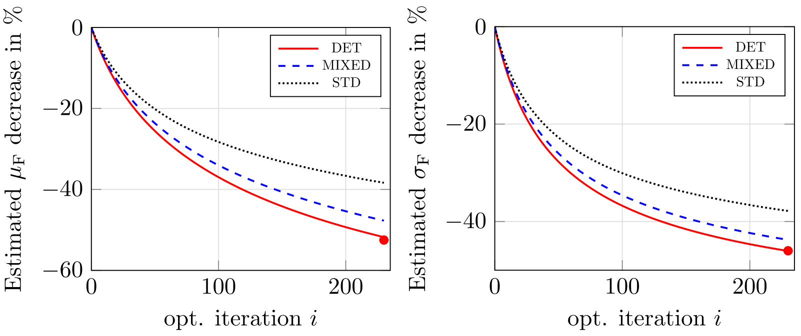

Fig. 5 Optimizations for uncertain hemolysis parameters. Left: FOSM-predicted decrease of the mean value of the QoI. Right: FOSM-predicted decrease of the standard deviation of the QoI. Filled circles denote the MC-predicted mean value and standard deviation decrease for DET (see Fig. 7)

case w.r.t. the hemolysis parameters. In view of these findings, the shape produced by the DET procedure is deemed as the general optimal solution out of the three. To this extent, it is further scrutinized w.r.t. the statistical moments of the QoI.

The FOSM method considers a linear relation between the QoI and the uncertain parameters. To evaluate the accuracy of this prediction throughout the optimization, additional MC simulations with a total sample size of $N = 1000$ are realized for the initial and optimized (DET) shapes. The samples are randomly selected using a normal distribution, for each uncertain variable, with a mean and standard deviation as the one employed by the FOSM-based optimizer. The results of the MC studies are shown in Fig. 7. The FOSM-predicted mean values of the initial and optimized shapes differ from the MC prediction by less than 6%. The standard deviation predictions differ by approximately 14%. Nevertheless, the underprediction of the statistical moments by the FOSM method is consistent for both initial and final shapes, thus resulting in an excellent prediction of the relative decrease of the statistical moments during the optimization process, as illustrated by the filled circles in Fig. 5.

Furthermore, it should be noted that based on the employed step size, all optimizations terminated due to the maximum iteration limit. Even though a small step size, as the one employed in this work, can slow down the optimization process, it guarantees that the process can continue uninterrupted. As discussed in Sect. 2, we employ a parameter-free shape optimization approach in which the deformation of the shape is realized directly on the level of the mesh. It is therefore important to the process that the meshes produced in the sequence sustain a certain level of their initial mesh quality. One of the ways to guarantee this property during the optimization is to employ a relatively small step size.

3.3.2 Uncertain non-Newtonian parameters

Figure 8 shows the FOSM-estimated decrease of the statistical moments of the QoI for the three optimization cases with uncertain non-Newtonian parameters. Two observations

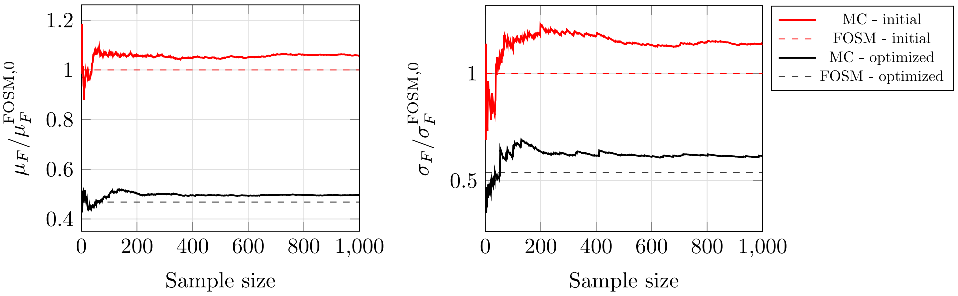

Fig. 7 MC study for uncertain hemolysis parameters. Left: running mean value of the QoI for the initial shape (red continuous line) and the optimized shape produced by DET (black continuous line) computed by the MC procedure with $N = 1000$. Right: running standard deviation of the QoI. Dashed lines denote the FOSM-predicted statistical moments for reference. Results are normalized by the FOSM-predicted mean value and standard deviation of the initial shape accordingly

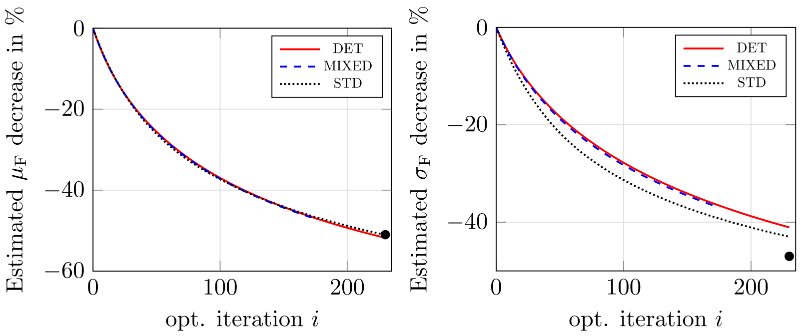

Fig. 8 Optimizations for uncertain non-Newtonian parameters. Left: FOSM-predicted decrease of the mean value of the QoI. Right: FOSM-predicted decrease of the standard deviation of the QoI. Filled circles denote the MC-predicted mean value and standard deviation decrease for DET (see Fig. 10)

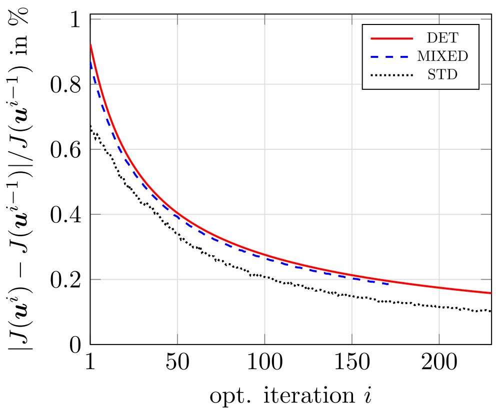

Fig. 9 Optimizations for uncertain non-Newtonian parameters. Relative change of the objective functional in percent for two subsequent shapes

of interest can be made for these results. First, it is shown that all three cases lead to a very similar optimization history w.r.t. the mean value of the QoI. Second, as regards the standard deviation relative decrease prediction, it is shown that the STD procedure shows the most prominent decrease in accordance to our expectations, since it targets exclusively the minimization of the standard deviation of the QoI. Specifically, the final shape obtained by the STD procedure results in approximately 43% decrease of the standard deviation of the QoI, while the DET procedure terminates at a decrease of approximately 40%. It is also interesting to note that the MIXED optimization run terminates abruptly after 172 optimization iterations due to mesh deformations that heavily deteriorated the quality of the grid, thus leading to the divergence of the primal solver. As in the case of uncertain hemolysis parameters, Fig. 9 shows the relative change of the objective functional. A similar convergence history is noted as in Sect. 3.3.1, with fluctuations, however, noted in the STD case. Overall, the results of the optimization runs suggest that the shape produced by STD exhibits the most beneficial behavior for both monitored statistical moments. In specific, the STD case managed to reduce the mean value of the QoI from $7.00 \cdot 10^{-8}$ to $3.43 \cdot 10^{-8}$ and the standard deviation from $1.25 \cdot 10^{-8}$ to $7.11 \cdot 10^{-9}$. To this end and similar to the case of uncertain hemolysis parameters, the shape produced by the STD procedure is further evaluated through an MC study with a sample size of $N = 1000$.

The results of the MC studies are shown in Fig. 10. The FOSM- and MC-predicted mean values differ by less than 6% for both initial and optimized shapes. The FOSM underprediction is again consistent for both shapes and the estimated decrease is thus accurately predicted by the FOSM method as shown by the filled circle in Fig. 8 (left). The standard deviation is significantly underpredicted by the FOSM approach with differences from the MC estimations of more than 35% for both initial and optimized shape. However, in terms of the relative decrease, the FOSM-prediction falls short by less than 5%.

3.3.3 Discussion on optimization results

For the scenario in which the hemolysis parameters are considered uncertain, the shape produced by the DET

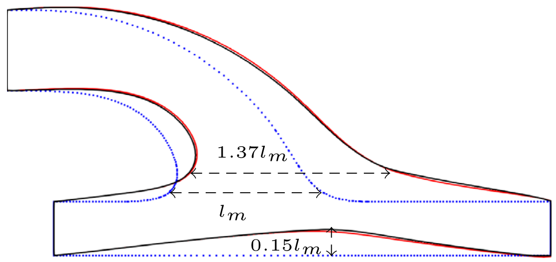

Fig. 11 Outlines of the initial shape (blue dots), optimized for uncertain hemolysis parameters and the DET procedure (red continuous line) and optimized for uncertain non-Newtonian parameters and the STD procedure (black continuous lines). Changes in the direction perpendicular to the main flow are trivial

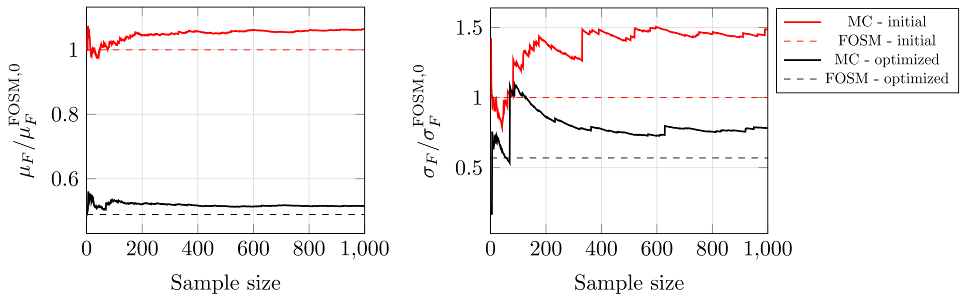

Fig. 10 MC study for uncertain non-Newtonian parameters. Left: running mean value of the QoI for the initial shape (red continuous line) and the optimized shape produced by STD (black continuous line) computed by the MC procedure with $N = 1000$. Right: running standard deviation of the QoI. Dashed lines denote the FOSM-predicted statistical moments for reference. Results are normalized by the FOSM-predicted mean value and standard deviation of the initial shape accordingly

optimization case was found to outperform the other two in reducing both statistical moments. The same holds for the shape produced by the STD optimization case for the scenario of uncertain non-Newtonian parameters. Figure 11 shows the outlines of the selected optimized shapes against the initial one. Both optimized shapes correspond to very similar designs with differences most prominent in the downstream region. The optimizer widened the anastomosis region, from heel to toe. Specifically, the characteristic length of the optimized cuff is increased by approximately 37%. This result was anticipated from the parametric results in Bletsos et al. (2024), where it was shown that a bypass graft with a large cuff resulted in smaller hemolysis potential predictions in comparison to grafts with a smaller cuff. In addition to this anticipated result, the optimized shape suggests that the bed region should be raised by a maximum of approximately $0.15 l_m$. While this raises questions as regards its practical implementation on a surgical procedure, there has already been biomedical interest in this direction as shown by the work of Rückert (2001).

As shown in Fig. 12, the optimized shapes result in a smoother transition of the blood flow from the implant to the artery. This results in a decrease of the flow shear stresses, as monitored by the scalar stress metric (Eq. (6)), which in turn results in the overall decrease of the potential induction of blood damage. These observations justify the minimization of the mean value of the QoI. At this point, we would like to emphasize the qualitative character of our study. The range of scalar stresses are indeed below experimentally measured values in which hemolysis induction takes place. Nevertheless, it is assumed that the flow characteristics remain similar even in flows of higher stresses and, thus, the presented optimized shapes are assumed to be beneficial to the hemodynamics, as regards their hemolysis potential, in a generalized context.

Furthermore, as shown by the optimization results and then validated by the corresponding MC studies, the reduction of the mean value is also accompanied by a reduction of the standard deviation of the QoI. This suggests that the two statistical moments are not of competitive nature and could be interdependent in the context of the application studied in this work. Based on this, we draw the conclusion that in the optimized shapes, a simulation employing an inconsistent set of parameters poses less risk of returning inaccurate predictions. While this might be medically irrelevant, it is important in the ever-growing field of computational biomedical studies, especially in the context of model parameters that are often hard to estimate in vivo applications. However, the studies presented herein suggest that the minimization of the mean value might often prove sufficient to also minimize uncertainties induced by the modeling process without the need for explicitly accounting for them.

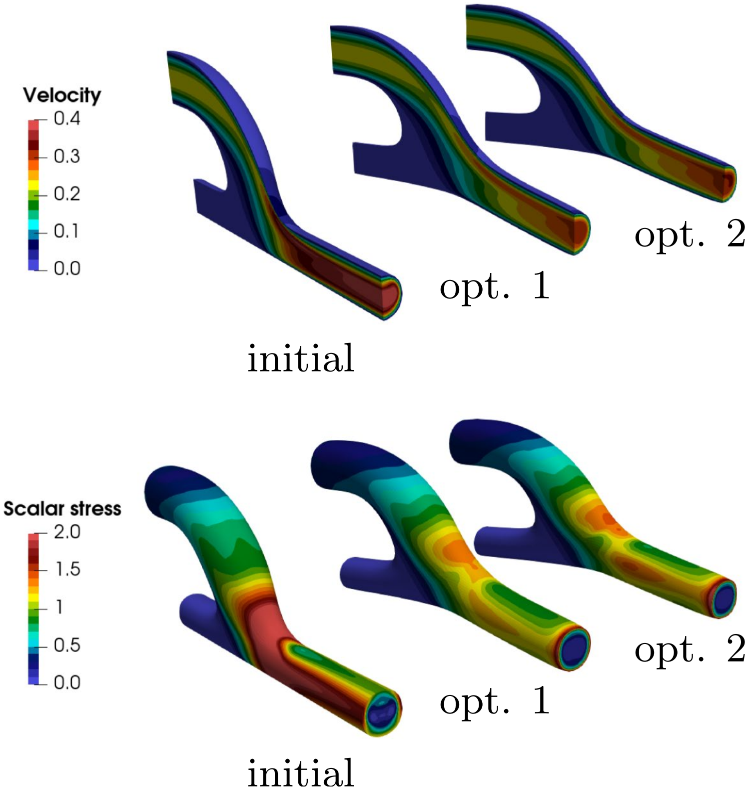

Fig. 12 Perspective view of the initial bypass graft and optimized for uncertain hemolysis parameters and the DET procedure (opt. 1) and uncertain non-Newtonian parameters and the STD procedure (opt. 2). Top: velocity magnitude contours in m/s. Bottom: scalar stress contours in Pa

3.3.4 FSI simulations of optimized shapes

The goal of this section is to evaluate the response of the optimized shapes under more realistic conditions. The initial shape was optimized under simplifying assumptions, such as steady-state conditions and rigid walls. To this extent, it is interesting to evaluate the performance of the optimized shapes with elastic walls and periodic inflow. The optimized shapes, denoted in Sect. 3.3.3 as opt. 1 and opt. 2, and their corresponding deformed grids are directly extracted from the optimization process. Based on the surface meshes, new structure domains are developed based on the procedure thoroughly described in Bletsos et al. (2024).

Even though the optimization studies accounted for non-Newtonian properties, the fluid properties are now set to $\tilde{\mu} = 4\,\mathrm{mPa}\cdot\mathrm{s}$ and $\rho = 10^3\,\mathrm{kg/m}^3$ to enable a direct comparison between the initial shape, evaluated with FSI in Bletsos et al. (2024) and the post-optimized shapes. Furthermore, an exercise flow pulse, which is generated by shortening the diastolic potion of the waveform (Fig. 3) by 0.25 s and scaling it accordingly, is prescribed. Employing an exercise flow pulse instead of the rest flow pulse is done, since it was previously found that it results to more critical hemolysis indexes and therefore enables a "worst-case scenario" simulation. Furthermore, a Womersley velocity profile (Womersley 1955) is prescribed on the inlet. The pressure on the outlet of the fluid domain is implicitly computed based on a three-element Windkessel model and the volume flux at the outlet. The simulation is realized for three cardiac cycles. For further details on the FSI simulation setup, the interested reader is pointed to Bletsos et al. (2024). A brief description of the employed partitioned FSI solution scheme employed is also included in "Appendix A" of this paper.

In addition to the hemolysis potential, for which the optimization process exclusively accounted for, it is interesting to monitor the oscillatory shear index (OSI)

$$\mathrm{OSI} = \frac{1}{2}\left(1 - \frac{\left\| \int_{T_\mathrm{o}} \tau_{ij} n_j \,\mathrm{d}t \right\|_2}{\int_{T_\mathrm{o}} \left\| \tau_{ij} n_j \right\|_2 \mathrm{d}t}\right), \tag{36}$$

where $\tau_{ij} n_j$ is evaluated on Γ_w and T_o denotes the last simulated cardiac cycle period. OSI is a hemodynamic metric of particular biomedical interest in bypass grafting due to its relation to the development of intimal hyperplasia. This quantity represents a spatial scalar field over Γ_w and becomes critical for values closer to the maximum value of 0.5. To characterize the complete optimized domains based on an index related to the OSI, the mean OSI over an observation region is further evaluated as

$$\text{mean OSI} = \frac{1}{A^\mathrm{o}} \int_{\Gamma^\mathrm{o}} \mathrm{OSI}\,\mathrm{d}\Gamma, \tag{37}$$

where A^o denotes the area of the observation section and Γ^o the observation surface. The observation area for the optimized shapes remain topologically the same as the one presented for the initial shape in Bletsos et al. (2024).

Furthermore, as regards the quantification of hemolysis in the context of an unsteady simulation, the QoI (Eq. (7)) is computed in each time iteration, and then, the complete simulation is assessed based on a time-averaged metric that reads

$$\mathrm{TAHI} = \frac{1}{T_\mathrm{o}} \int_{T_\mathrm{o}} F\,\mathrm{d}t. \tag{38}$$

Figure 13 presents the investigated metrics for the initial and optimized shapes. The time-averaged hemolysis index is decreased by approximately 41% and 37% for the opt. 1 and opt. 2 shapes, respectively, in comparison to the initial. The decrease of this index of interest is consistent with the results of the optimization, in the sense that the opt. 1 shape resulted in a slightly larger decrease of the mean value of the QoI in comparison to opt. 2. Furthermore, it is worth noting that a decrease of approximately 9% was reported in Bletsos et al. (2024) when parametrically changing the shape. Therefore, our findings herein highlight the potential of formal shape optimization procedures in biomedical applications, even when these are applied in a simplified manner (e.g., steady-state conditions and rigid walls).

As regards OSI, it is shown that the decrease of TAHI is accompanied by an increase of the mean OSI by approximately 44% for the opt. 1 shape and 41% for the opt. 2 shape. This finding validates our previous observations regarding the competitive nature between hemolysis and OSI. The consistent trend between OSI and hemolysis necessitates the inclusion of the latter in the formulation of the optimization

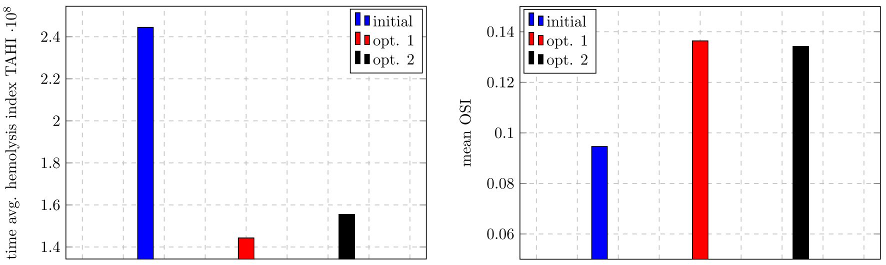

Fig. 13 Comparison of TAHI and mean OSI on the initial bypass graft (results extracted from Bletsos et al. (2024)) and on the optimized shapes using FSI simulations for exercise conditions and a Womersley inlet velocity profile

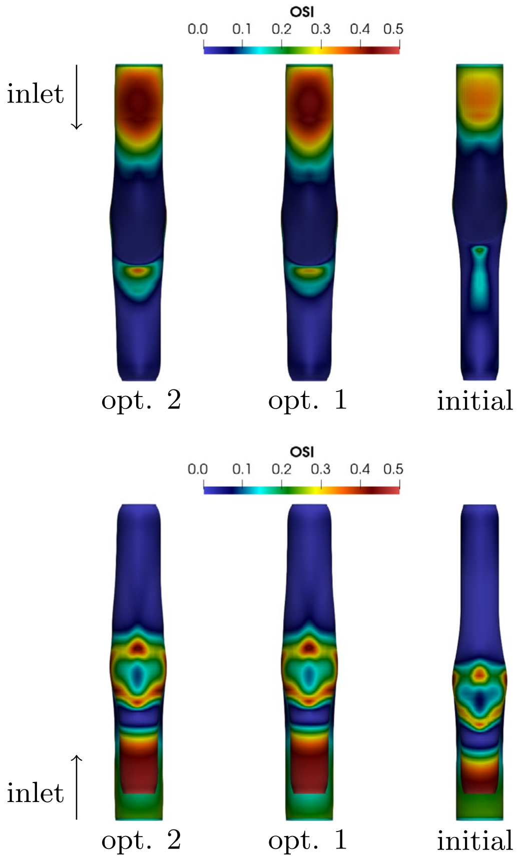

Fig. 14 Comparison of OSI fields on initial (results extracted from Bletsos et al. (2024)) and optimized shapes. Top: top view of the bypass grafts. Bottom: bottom view of the bypass grafts

problem, either by means of a constraint of by means of a weighted average of the two quantities.

The increase of the mean OSI metric is further scrutinized in Fig. 14. It is shown that the OSI ring initially observed around the bed region and cuff region attains higher values of OSI on the optimized shapes. Concurrently, the toe region of the anastomosis exhibits a wider area of more critical OSI values in comparison to the initial. These results explain the overall increase of the mean OSI in the optimized shapes.

4 Summary and conclusions

This paper presented the robust shape optimization of an idealized arterial bypass graft. The problem was considered uncertain by means of the parameters used to model hemolysis or the non-Newtonian properties of blood. We considered a hemolysis index on the outlet of the domain as our QoI. The FOSM method was used to propagate the uncertainties of the underlying state to the QoI. Based on this, an adjoint-assisted parameter-free shape optimization problem was formulated in a gradient-based manner. The method was applied for each set of uncertain parameters independently and for three sets of weights of the statistical moments of the QoI, thus amounting to a total of five optimization runs. Additional MC simulations were conducted to evaluate the accuracy of the FOSM-based predictions. The optimization studies suggested two designs as overall optimal candidates, able to decrease the mean value of the hemolysis index by approximately 50%. Due to the simplifying assumptions employed to enable computationally feasible optimization runs, the selected designs were subsequently assessed under more physiological unsteady FSI conditions. It was found that the steady-state optimized shapes result in significant decreases of up to 41% for hemolysis even on the unsteady, elastic walls setting. The key findings of this paper are summarized as follows:

- Uncertainties on the hemolysis or non-Newtonian properties are found to be relatively trivial in the context of the shape optimization studies conducted herein. Specifically, it is shown that an optimization targeting exclusively the minimization of the mean value also decreases the standard deviation of the hemolysis index. However, it was found that in the case of uncertain non-Newtonian parameters, an optimization exclusively of the standard deviation can further increase the robustness of the shape against uncertain parameters.
- The FOSM-based predictions of the statistical moments of hemolysis are found to be fairly accurate in the context of relative evaluations while fall short on absolute predictions, as shown by the accompanying MC simulations.
- The optimized shapes suggest a widening of the cuff region and a lift of the impaired artery so that to smoothen the transition of the blood flow from the graft to the artery.
- Even under the more physiologically relevant unsteady conditions with elastic graft and artery walls, the optimized shapes are found to outperform the initial shape. This finding suggests that a reduced optimization formulation can provide significant clinically relevant results at a feasible computational cost.
- A competitive relation between OSI and hemolysis induction w.r.t. the shape was found. This finding is in agreement to our previous observations in Bletsos et al. (2024).

We identify as a limitation of this work its qualitative nature due to the idealized geometry as well as the simplifying assumptions, e.g., rigid walls, steady-state flow, and Poiseuille inlet velocity profile, employed for the optimization studies. We also acknowledge a certain level of ambiguity as regards the choice of mean values and standard deviations of the uncertain variables due to a lack of experimental data in virtue of the complexity of the investigated case. To this extent, we are working toward a) applying the presented numerical methodology in blood pumps based on which the simulations can later be experimentally validated and b) investigating patient-specific arterial bypass graft geometries associated with post-surgery clinical data.

Appendix A: Partitioned FSI solution scheme

For the realization of the FSI simulations, the fluid problem needs to be formulated based on an Arbitraty–Lagrangian–Eulerian (ALE) viewpoint (Donea et al. 2004) and it must be coupled with the conservation laws of the structure.

Briefly, the ALE description of the fluid results in the reformulation of the convective term of a transported quantity ϕ

$$\text{from} \quad v_j \frac{\partial \phi}{\partial x_j} \quad \text{to} \quad \left(v_j - \tilde{v}_j\right) \frac{\partial \phi}{\partial x_j}, \tag{A1}$$

where $\tilde{v}_j$ refers to the domain velocity vector components. In this work, the domain velocity is implicitly determined based on the swept volume approach (Ferziger et al. 2020) and a corresponding correction of the volume fluxes.

The structure subproblem reduces to the conservation of momentum. A weak form of the conservation equation is discretized using higher-order finite elements. The solution of the structure subproblem is the displacement vector of the structure, i.e., d_j^{s}. As constitutive models, we employ a nearly incompressible Fung material for the arterial wall and a compressible Neo-Hooke model for the graft. A detailed presentation of the modeling and simulation approach for the structure subproblem is given in Bletsos et al. (2024). All structure simulations are done using the high-order finite element framework *AdhoC* (see Zander et al. 2014).

In addition to the boundary conditions required for each subproblem, the FSI problem demands that the following coupling conditions are fulfilled on the coupling interface, which in our cases stands for $\Gamma_{\mathrm{t}}^{\mathrm{FSI}} \equiv \Gamma_{\mathrm{w}}$

$$v_j = \tilde{v}_j = \dot{d}_j^{\mathrm{s}} \quad \text{on } \Gamma_{\mathrm{t}}^{\mathrm{FSI}} \tag{A2}$$

$$t_j = -\left(2\tilde{\mu} S_{ij} - p\delta_{ij}\right) n_i \quad \text{on } \Gamma_{\mathrm{t}}^{\mathrm{FSI}}, \tag{A3}$$

where t_j stands for the components of the traction vector. Equations (A2) and (A3) are enforced through a partitioned solution scheme, which considers the individual field solvers as black boxes. Specifically, Eq. (A2) refers to the transmission of information from the structure to the fluid, while Eq. (A3) from the fluid to the structure. This is illustrated by an operator formulation, where

$$D_{ji}^t = \mathcal{S}(T_{ki}^t) \quad \text{for } j = 1, \ldots, \mathrm{N}^{\mathrm{fc}} \quad \text{and } k = 1, \ldots, \mathrm{N}^{\mathrm{qp}} \tag{A4}$$

denotes the solution at the time step t of the structure subproblem, which yields D_{ji}^t given the tractions T_{ki}^t. The former represents a matrix of N^{fc} rows where each row contains the displacement vector d_i^{s} computed at one discrete face center of $\Gamma_{\mathrm{t}}^{\mathrm{FSI}}$, where N^{fc} is used to denote the total number of discrete fluid faces on the interface. Equivalently, T_{ki}^t contains at each row the traction vector t_i for one quadrature point discretizing the structure domain, where N^{qp} is used to denote the total number of discrete structure elements on the interface. Similarly, one can write

$$T_{ki}^t = \mathcal{F}(D_{ji}^t) \quad \text{for } j = 1, \ldots, \mathrm{N}^{\mathrm{fc}} \quad \text{and } k = 1, \ldots, \mathrm{N}^{\mathrm{qp}}, \tag{A5}$$

to represent the fluid subproblem solution. In a coupled problem, it must hold

$$D_{ji}^t = \mathcal{S}(\mathcal{F}(D_{ji}^t)) \quad \text{and} \quad T_{ki}^t = \mathcal{F}(\mathcal{S}(T_{ki}^t)). \tag{A6}$$

A solution to these fixed-point equations can be found using an accelerated fixed-point iteration with the following three steps:

$$\begin{aligned} T_{ki}^{t,l} &= \mathcal{F}(D_{ji}^{t,l-1}) && \text{1. call fluid solver} \\ \tilde{D}_{ji}^{t,l} &= \mathcal{S}(T_{ki}^{t,l}) && \text{2. call structure solver} \\ D_{ji}^{t,l} &= \mathcal{A}(\tilde{D}_{ji}^{t,l}) && \text{3. accelerate convergence,} \end{aligned}$$

where l is used to indicate the coupling iteration and $\tilde{D}_{ji}^{t,l}$ is used to denote an intermediate solution of the structure solver. The acceleration operator $\mathcal{A}$ introduced as a third step of the algorithmic process might refer to a wide variety of choices. In this work, the Quasi-Newton least-squares (QNLS) method (see Degroote et al. 2009) is used to accelerate the convergence. We employ the filtering technique from Haelterman et al. (2016) in combination with the resetting technique introduced in Radtke et al. (2016). The iterative solution of the FSI problem is realized with the use of the coupling tool *comana* (König et al. 2016).

Appendix B: Derivation of the adjoint system

The core building blocks of the continuous adjoint system employed in this study refer to the incorporation of the primal hemolysis and non-Newtonian viscosity equations in the adjoint derivation process. These can be separately found in

Bletsos et al. (2021) and Bletsos et al. (2023), respectively. The adjoint system (Eqs.(17)-(20)) considers the combination of both hemodynamic aspects and, therefore, cross-coupling terms need to be considered. A Lagrangian functional for the problem at hand can be stated as

$$\mathcal{L} = \tilde{F} + \int_\Omega \left(\hat{p}R^p + \hat{v}_i R_i^v + \hat{h}R^H + \hat{\mu}R^{\tilde{\mu}}\right) \mathrm{d}\Omega, \tag{B7}$$

where $\tilde{F}$ denotes exclusively the numerator of the QoI (see, Eq. (7)), since the denominator remains constant throughout the optimization, under the employed assumptions of an incompressible fluid and non-moving inlet and outlet boundaries. In addition, we use $R^{\tilde{\mu}}$ to denote the constraining primal algebraic non-Newtonian viscosity equation, which for the employed Carreau model reads

$$R^{\tilde{\mu}} = \tilde{\mu} - \mu_\infty + (\mu_0 - \mu_\infty)(1 + (\lambda\dot{\gamma})^2)^{\frac{n-1}{2}} = 0. \tag{B8}$$

The additional cross-coupling terms are introduced based on the directional derivatives $\delta_{H_L} R_i^v \cdot \delta H_L$, $\delta_{H_L} R^{\tilde{\mu}} \cdot \delta H_L$, $\delta_{\tilde{\mu}} R^H \cdot \delta\tilde{\mu}$. However, due to the one-way coupling of the employed hemolysis model to the flow equations, both $\delta_{H_L} R_i^v \cdot \delta H_L$ and $\delta_{H_L} R^{\tilde{\mu}} \cdot \delta H_L$ identically vanish. Therefore, the only additional contribution is

$$\begin{aligned}\delta_{\tilde{\mu}} R^H \cdot \delta\tilde{\mu} &= \cancelto{0}{\delta_{\tilde{\mu}}\left(v_j \frac{\partial H_L}{\partial x_j}\right)} \cdot \delta\tilde{\mu} - \delta_{\tilde{\mu}}\left(C^{\frac{1}{\beta}} \bar{\tau}^{\frac{\alpha}{\beta}} (1 - H_L)\right) \cdot \delta\tilde{\mu} \\ &= -\left(2\frac{\alpha}{\beta}\tilde{\mu} C^{\frac{1}{\beta}} (1 - H_L) \bar{\tau}^{\left(\frac{\alpha}{\beta}-2\right)} S_{ij} S_{ij}\right) \cdot \delta\tilde{\mu}.\end{aligned} \tag{B9}$$

The construction of the field adjoint viscosity equation is now based on the optimality condition

$$\begin{aligned}\delta_{\tilde{\mu}}\mathcal{L} \cdot \delta\tilde{\mu} &= \int_\Omega \left(\boxed{\hat{v}_i\left(\delta_{\tilde{\mu}} R_i^v \cdot \delta\tilde{\mu}\right) + \hat{\mu}\left(\delta_{\tilde{\mu}} R^{\tilde{\mu}} \cdot \delta\tilde{\mu}\right)} + \hat{h}\left(\delta_{\tilde{\mu}} R^H \cdot \delta\tilde{\mu}\right) \right) \mathrm{d}\Omega \\ &= \int_\Omega \left(\boxed{\hat{\mu} + 2S_{ij}\frac{\partial \hat{v}_i}{\partial x_j}} - \underbrace{2\hat{h}\frac{\alpha}{\beta}\tilde{\mu} C^{\frac{1}{\beta}} \left(1 - H_L\right) \bar{\tau}^{\left(\frac{\alpha}{\beta}-2\right)} S_{ij} S_{ij}}_{\Lambda} \right) \cdot \delta\tilde{\mu}\, \mathrm{d}\Omega \\ &= \int_\Omega \left((\hat{\mu} - \Lambda) + 2S_{ij}\frac{\partial \hat{v}_i}{\partial x_j} \right) \cdot \delta\tilde{\mu}\, \mathrm{d}\Omega \, := 0,\end{aligned} \tag{B10}$$

which is satisfied for every $\delta\tilde{\mu}$ by the solution of the adjoint equation (20). Note that in the derivations of Eq. (B10), the boxed terms have previously been derived in Bletsos et al. (2023). The remaining other adjoint equations do not include any further additional cross-coupling terms.

Verification of first-order derivative w.r.t. the control

The proposed sensitivity for the determination of the first-order derivative w.r.t. the control, see Eq. (25), which considers the combination of both adjoint hemolysis and non-Newtonian properties can be assessed by means of a second-order accurate finite differences study. The geometry considered for this study refers to a 2D symmetrically stenosed duct, as schematically shown in Fig. 15. Therein, Γ_d is used to denote the section in which the finite differences study is conducted.

The shape of the stenosis on the bottom wall follows from:

$$y = \delta^* \left(\sin\left(\frac{\pi}{L_\mathrm{d}} x - \frac{\pi}{1000} \right) \right)^4, \quad \forall x \in [L_\mathrm{w}, L_\mathrm{w} + L_\mathrm{d}], \tag{B11}$$

where δ^* is the height of the bump and amounts to $\delta^* = \mathrm{H}^*/3$, with $\mathrm{H}^* = 15\,\mathrm{mm}$ denoting the total height of the duct, $L_\mathrm{w} = 500\,\mathrm{mm}$ refers to the distance of the inlet and outlet to the start of the bump and $L_\mathrm{d} = 100\,\mathrm{mm}$ denotes the length of the bump. The geometry is discretized with approximately 67000 control volumes with an average dimensionless near-wall spacing on Γ_d of $y^+ \approx \mathcal{O}(10^{-2})$ for the flow conditions employed in this study. On the leftmost inlet boundary patch, a parabolic Poiseuille velocity profile is set, viz.

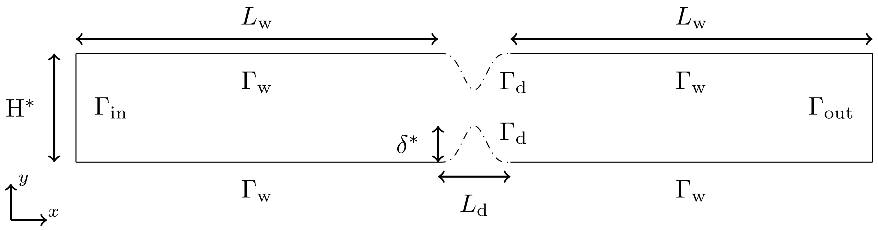

Fig. 15 Sketch of the 2D double-stenosed geometry. The origin coincides with the leftmost lowest point of the geometry. Dashed lines correspond to the design section (Γ_d)

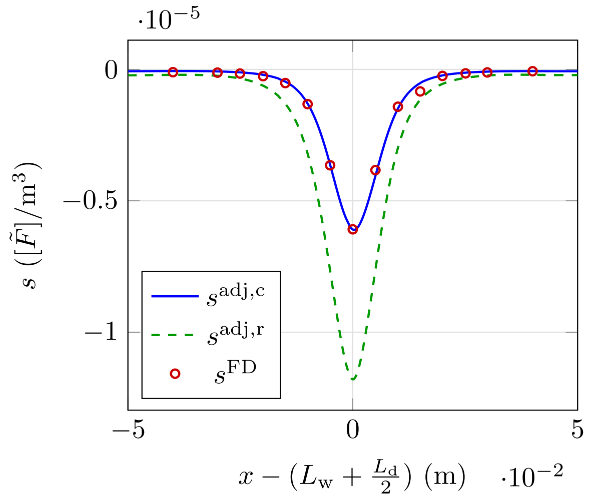

Fig. 16 Sensitivity estimations based on the proposed expression of Eq. (25) (continuous blue line, $s^{\mathrm{adj,c}}$), a reduced adjoint and sensitivity formulation neglecting the additional cross-coupling terms (dashed green line, $s^{\mathrm{adj,r}}$) and the finite differences method for $\epsilon_{\mathrm{fd}} = \delta^* \cdot 10^{-5}$

$$v_x^{\mathrm{in}} = 2\,V\left(1 - \left(\frac{2y - \mathrm{H}^*}{\mathrm{H}^*}\right)^2\right), \tag{B12}$$

with $V = 6.6\,\mathrm{mm/s}$. A zero pressure condition is used for the downstream vertical outlet boundaries and all the walls follow a no-slip boundary condition. The properties of the fluid are set to $\rho = 1056\,\mathrm{kg/m}^3$, while the viscosity follows from the Carreau model, cf. Eq. (4), with parameters fixed to $\left(\lambda, n, \mu_0, \mu_\infty\right) = (3.313\,\mathrm{s}, 0.357\,[-], 56\,\mathrm{mPa}\cdot\mathrm{s}, 3.5\,\mathrm{mPa}\cdot\mathrm{s})$. As regards hemolysis modeling, cf. Eq. (5), the study employs the set of constants $(C, \alpha, \beta) = \left(3.6 \cdot 10^{-7}, 2.416, 0.785\right)$. To evaluate the derived adjoint sensitivity expression, the study monitors

$$\tilde{F} = \int_{\Gamma_{\mathrm{out}}} H v_i n_i \,\mathrm{d}\Gamma. \tag{B13}$$

The finite differences study is realized by perturbing individual faces of the bottom discretized design section, indicated by L_d in Fig. 15, in their normal direction $\boldsymbol{n}^{\mathrm{F}}$. The center and corresponding nodes of each discrete face is perturbed in both positive and negative normal directions by ϵ_{fd} to facilitate a second-order accurate derivative approximation. Once the finite differences simulations are converged, the local surface sensitivity is estimated for a discrete surface patch with coordinates $\boldsymbol{u}^{\mathrm{F}}$ as

$$s^{\mathrm{F,\,FD}} = \frac{[\tilde{F}(\boldsymbol{u}^{\mathrm{F}} + \epsilon_{\mathrm{fd}}\,\boldsymbol{n}^{\mathrm{F}}) - \tilde{F}(\boldsymbol{u}^{\mathrm{F}} - \epsilon_{\mathrm{fd}}\,\boldsymbol{n}^{\mathrm{F}})]}{2\epsilon_{\mathrm{fd}}}\,\frac{1}{\Delta\Gamma^{\mathrm{F}}}, \tag{B14}$$

where $\Delta\Gamma^{\mathrm{F}}$ denotes area of the perturbed face.

In addition to the finite differences study, we simulate two adjoint scenarios. The first considers the complete adjoint system as introduced in Sect. 2.3.1 and the sensitivity is estimated based on Eq. (25). The second corresponds to a reduced formulation which neglects the cross-coupling terms from both the adjoint system and the sensitivity expression, i.e., $\Lambda = 0$. Figure 16 compares the sensitivity results obtained from the finite differences study (open symbols) with the results of the two adjoint approaches. As shown there, the results obtained from Eq. (25), represented by the straight line, agree satisfactorily with the finite difference results. Contrary, when the additional cross-coupling terms are dropped, the resulting sensitivity represented by the dashed line significantly disagrees with the finite difference sensitivity.

Appendix C: Sensitivity analysis of uncertain parameters

The FOSM method is based on a first-order Taylor series expansion of the QoI around the mean values of the uncertain variables, and thus, the approximation becomes accurate when the QoI is linear to the uncertain parameters in a neighborhood close to their means, cf. Equation (9). Therefore, it is interesting to preliminary evaluate the response of the QoI (Eq. (7)) w.r.t. variations of the uncertain variables around their mean values. To this end, the initial shape of the optimization studies presented

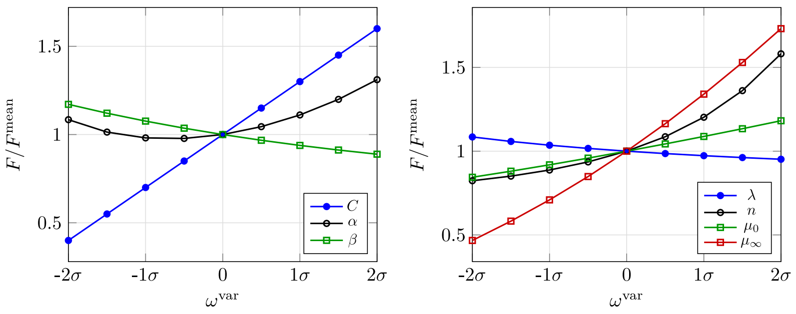

Fig. 17 Response of the QoI (Eq. (7)) w.r.t. variations of the uncertain variables around their mean values. The mean value and standard deviation of each uncertain parameters refer to Eqs. (32) and (34). Normalization of the QoI based on the QoI evaluated for all parameters set to the mean values, F^{mean}. Left: variations of the hemolysis parameters. Right: variations of the non-Newtonian model parameters

in Sect. 3 is evaluated for perturbed values of uncertain variables.

The study considers the hemolysis and non-Newtonian model parameters to be fixed to the mean values presented in Eqs. (32) and (34), respectively. Each one of them is then perturbed in 8 steps by $\omega^{\text{var}} = (-2\sigma, -1.5\sigma, -1\sigma, -0.5\sigma, 0.5\sigma, 1\sigma, 1.5\sigma, 2\sigma)$, where σ refers to the standard deviation considered for each uncertain variable, while the rest remains fixed. The QoI is then monitored and presented in Fig. 17.

As indicated by the figure, the QoI exhibits an almost linear response for most uncertain parameters, except for α (hemolysis parameter) and n (non-Newtonian parameter). In view of these results and considering the additional computations that a higher-order method of moments would require, the FOSM method is deemed as an acceptable UQ strategy for the problem at hand. However, note that the study herein is conducted only for the initial shape and the response of the QoI w.r.t. perturbations of the uncertain variables might change during the shape optimization process.

Acknowledgements The current work is part of the research training group 'Simulation-Based Design Optimization of Dynamic Systems Under Uncertainties' (SENSUS) funded by the state of Hamburg within the Landesforschungsförderung under Project No. LFF-GK11. The authors gratefully acknowledge the computing time made available to them on the high-performance computers Lise and Emmy at the NHR centers ZIB and Göttingen under the project "Adjoint Optimization for Applications in Hemodynamics" (hhi00034). These centers are jointly supported by the German Federal Ministry of Education and Research and the state governments participating in the NHR (www.nhr-verein.de/unsere-partner). The second author gratefully acknowledges the support of the DFG (Deutsche Forschungsgemeinschaft) under DU 405/20-1 (Grant No. 503865803). Finally, the authors would like to thank the two anonymous reviewers for their very constructive feedback on earlier versions of this article.

Author contributions GB: conceptualization, formal analysis, investigation, methodology, software, validation, visualization, writing—original draft, and writing—review and editing. LR: methodology, software, supervision, and writing—review and editing. TR: conceptualization, funding acquisition, methodology, project administration, resources, supervision, and writing—review and editing.

Funding Open Access funding enabled and organized by Projekt DEAL. This research is funded by the state of Hamburg within the Landesforschungsförderung under Project No. LFF-GK11. Additionally, the second author is funded by DFG (Deutsche Forschungsgemeinschaft) under DU 405/20-1 (Grant No. 503865803).

Declarations

Conflict of interest On behalf of all authors, the corresponding author states that there is no conflict of interest.

Replication of results The results presented in Sect. 3.3 can be obtained by implementation of Algorithm 1, which can be provided upon reasonable request. The algorithm can support any commercial/open-source CFD software able to solve the primal, adjoint and descent direction problems presented in this paper. The initial discretized geometry of the graft can be created following the generalized methodology presented in Bletsos et al. (2024) due to its idealized shape. The initial and optimized geometries can be provided upon request. Results presented in Sect. 3.3.4 can be obtained by applying the partitioned FSI solution methodology thoroughly presented in our previous publication (Bletsos et al. 2024) and briefly outlined in "Appendix A". A detailed description of the design of the coupling software *comana* is provided in König et al. (2016). All data produced by the numerical experiments presented in this paper can be made available upon reasonable request.

References

Allaire G, Dapogny C, Jouve F (2021) Shape and topology optimization. In: Geometric partial differential equations, part II. Handbook of numerical analysis, vol. 22, pp. 1–132. Elsevier, Amsterdam

Bäck T (1996) Evolutionary algorithms in theory and practice. evolution strategies, evolutionary programming, genetic algorithms. Oxford University Press, NY

Brezillon J, Gauger NR (2004) 2d and 3d aerodynamic shape optimisation using the adjoint approach. Aerosp Sci Technol 8(8):715–727

Bazilevs Y, Hsu MC, Zhang Y, Wang W, Kvamsdal T, Hentschel S, Isaksen JG (2010) Computational vascular fluid-structure interaction: methodology and application to cerebral aneurysms. Biomech Model Mechanobiol 9(4):481–498

Bletsos G, Kühl N, Rung T (2021) Adjoint-based shape optimization for the minimization of flow-induced hemolysis in biomedical applications. Eng Appl Comput Fluid Mech 15(1):1095–1112

Bletsos G, Kühl N, Rung T (2023) Adjoint shape sensitivities of blood flows considering non-Newtonian properties. Int J Numer Methods Fluids 95(11):1791–1819

Blair GWS (1959) An equation for the flow of blood, plasma and serum through glass capillaries. Nature 183(4661):613–614

Bletzinger K-U (2014) A consistent frame for sensitivity filtering and the vertex assigned morphing of optimal shape. Struct Multidisc Optim 49:873–895

Bletsos G, Rung T, Radtke L (2024) Hemodynamics in arterial bypass graft anastomoses with varying cuff sizes and proximal flow paths: a fluid-structure interaction study. Comput Methods Biomech Biomed Eng 28(7):1066–1085

Bazilevs Y, Takizawa K, Tezduyar TE (2013) Computational fluid-structure interaction: methods and applications. Wiley series in computational mechanics. John Wiley and Sons, Chichester

Chatterjee T, Chakraborty S, Chowdhury R (2019) A critical review of surrogate assisted robust design optimization. Arch Comput Methods Eng 26(1):245–274

Degroote J, Bathe KJ, Vierendeels J (2009) Performance of a new partitioned procedure versus a monolithic procedure in fluid-structure interaction. Comput Struct 87(11):793–801

Donea J, Huerta A, Ponthot JP, Rodríguez-Ferran A (2004) Arbitrary Lagrangian-Eulerian Methods. Chap, John Wiley and Sons Ltd, Chichester, p 14

Fragkos KB, Papoutsis-Kiachagias EM, Giannakoglou KC (2019) pfosm: an efficient algorithm for aerodynamic robust design based on continuous adjoint and matrix-vector products. Comput Fluids 181:57–66

Farhikhteh ME, Papoutsis-Kiachagias EM, Giannakoglou KC (2023) Aerodynamic shape optimization of wind turbine rotor blades using the continuous adjoint method. Optim Eng

Ferziger JH, Peric M, Street RL (2020) Computational methods for fluid dynamics, 4th edn. Springer, Cham

Fung Y-C (1993) 3. Biomechanics: mechanical properties of living tissues, pp. 66–108. Springer, New York, NY

Garon A, Farinas M (2004) Fast three-dimensional numerical hemolysis approximation. Artif Org 28(11):1016–1025

Goubergrits L, Kertzscher U, Lommel M (2018) Past and future of blood damage modelling in a view of translational research. Int J Artifl Org 42(3):125–132

Giannakoglou KC, Papadimitriou DI, Kampolis IC (2006) Aerodynamic shape design using evolutionary algorithms and new gradient-assisted metamodels. Comput Methods Appl Mech Eng 195(44):6312–6329

Giersiepen M, Wurzinger LJ, Opitz R, Reul H (1990) Estimation of shear stress-related blood damage in heart valve prostheses: in vitro comparison of 25 aortic valves. Int J Artif Org 13(5):300–306

Habibi M, Aslan S, Liu X, Loke Y, Krieger A, Hibino N, Olivieri L, Fuge M (2025) Automatic Laplacian-based shape optimization for patient-specific vascular grafts. Comput Biol Med 184:109308

Haelterman R, Bogaers AEJ, Scheufele K, Uekermann B, Mehl M (2016) Improving the performance of the partitioned qn-ils procedure for fluid-structure interaction problems: filtering. Comput Struct 171(Supplement C):9–17

Hsu MC, Kamensky D, Bazilevs Y, Sacks MS, Hughes TJR (2014) Fluid-structure interaction analysis of bioprosthetic heart valves: significance of arterial wall deformation. Comput Mech 54(4):1055–1071

Heuser G, Opitz R (1980) A couette viscometer for short time shearing of blood. Biorheology 17:17–24

Janssen H (2013) Monte-Carlo based uncertainty analysis: sampling efficiency and sampling convergence. Reliab Eng Syst Saf 109:123–132

Jiang D, Han D, Hu X (2016) The shape optimization of the arterial graft design by level set methods. Appl Math J Chin Univ 31(2)

Jahangirian A, Shahrokhi A (2011) Aerodynamic shape optimization using efficient evolutionary algorithms and unstructured CFD solver. Comput Fluids 46(1):270–276 (10th ICFD Conference Series on Numerical Methods for Fluid Dynamics (ICFD 2010))

Katsapoxaki P, Hottois R, Tran T-S, Schram C, Coussement G, Verstraete T (2023) Adjoint-based aeroacoustic optimization of NASA Rotor37. Turbo Expo: Power for Land, Sea, and Air, vol. 13C: Turbomachinery - Deposition, Erosion, Fouling, and Icing; Design Methods and CFD Modeling for Turbomachinery; Ducts, Noise, and Component Interactions, pp. 13–33010

Krüger JC, Kranz M, Schmidt T, Seifried R, Kriegesmann B (2023) An efficient and non-intrusive approach for robust design optimization with the first-order second-moment method. Comput Methods Appl Mech Eng 414:116136

Kriegesmann B, Lüdeker JK (2019) Robust compliance topology optimization using the first-order second-moment method. Struct Multidisc Optim 60(1)

Kranz M, Lüdeker JK, Kriegesmann B (2023) A generalized approach for robust topology optimization using the first-order second-moment method for arbitrary response functions. Struct Multidisc Optim 66(5)

Kühl N, Müller PM, Stück A, Hinze M, Rung T (2019) Decoupling of control and force objective in adjoint-based fluid dynamic shape optimization. AIAA J 57(9):4110–4114

Kühl N, Nguyen TT, Palm M, Jürgens D, Rung T (2022) Adjoint node-based shape optimization of free-floating vessels. Struct Multidisc Optim 65

Kröger J, Rung T (2015) CAD-free hydrodynamic optimisation using consistent Kernel-based sensitivity filtering. Ship Technol Res 62(3):111–130

König M, Radtke L, Düster A (2016) A flexible C++ framework for the partitioned solution of strongly coupled multifield problems. Comput Math Appl 72(7):1764–1789

Marsden AL (2014) Optimization in cardiovascular modeling. Ann Rev Fluid Mech 46(1):519–546

Morokoff WJ, Caflisch RE (1995) Quasi-Monte Carlo integration. J Comput Phys 122(2):218–230

Müller PM, Kühl N, Sieberborn M, Deckelnick K, Hinze M, Rung T (2021) A novel p-harmonic descent approach applied to fluid dynamic shape optimization. Struct Multidisc Optim 64(6):3489–3503

Nocedal J, Wright SJ (2006) Numerical optimization, 2e edn. Springer, New York

Othmer C (2008) A continuous adjoint formulation for the computation of topological and surface sensitivities of ducted flows. Int J Numer Methods Fluids 58:861–877

Papadimitriou DI, Giannakoglou KC (2013) Third-order sensitivity analysis for robust aerodynamic design using continuous adjoint. Int J Numer Methods Fluids 71(5):652–670

Papoutsis-Kiachagias EM, Asouti VG, Giannakoglou KC, Gkagkas K, Shimokawa S, Itakura E (2019) Multi-point aerodynamic shape optimization of cars based on continuous adjoint. Struct Multidisc Optim 59:675–694

Papoutsis-Kiachagias EM, Giannakoglou KC (2016) Continuous adjoint methods for turbulent flows, applied to shape and topology optimization: industrial applications. Arch Comput Methods Eng 23:255–299

Papoutsis-Kiachagias EM, Papadimitriou DI, Giannakoglou KC (2012) Robust design in aerodynamics using third-order sensitivity analysis based on discrete adjoint. Application to quasi-1d flows. Int J Numer Methods Fluids 69(3):691–709

Quarteroni A, Tuveri M, Veneziani A (2000) Computational vascular fluid dynamics: problems, models and methods. Comput Vis Sci 2:163–197

Rückert RI (2001) Experimentelle und klinische Untersuchungen zur Optimierung der Hämodynamik in termino-laterial Prothesenbypass-Anastomosen. Postdoctoral thesis, Medizinischen Fakultät Charié, Humboldt-Universität zu Berlin

Radtke L, Bletsos G, Kühl N, Suchan T, Rung T, Düster A, Welker K (2023) Parameter-free shape optimization: Various shape updates for engineering applications. Aerospace 10(9)

Radtke L, Larena-Avellaneda A, Debus ES, Düster A (2016) Convergence acceleration for partitioned simulations of the fluid-structure interaction in arteries. Comput Mech 57(6):901–920

RRA Martins J, T Hwang J (2013) Review and unification of methods for computing derivatives of multidisciplinary computational models. AIAA J 51(11)

Rung T, Wöckner K, Manzke M, Brunswig J, Ulrich C, Stück A (2009) Challenges and perspectives for maritime CFD applications. Jahrbuch der Schiffbautechnischen Gesellschaft 103:127–139

Shibeshi SS, Collins WE (2005) The rheology of blood flow in a branched arterial system. Appl Rheol 15(6):398–405

Shepard D (1968) A two-dimensional interpolation function for irregularly-spaced data. In: Proceedings of the 1968 23rd ACM national conference, pp. 517–524. Advancing computing as a science and profession, New York

Stück A, Rung T (2013) Adjoint complement to viscous finite-volume pressure-correction methods. J Comput Phys 248:402–419

Thamsen B, Blümel B, Schaller J, Paschereit CO, Affeld K, Goubergrits L, Kertzscher U (2015) Numerical analysis of blood damage potential of the HeartMate II and HeartWare HVAD rotary blood pumps. Artif Org 39(8):651–659

Upadhyay BD, Sonigra SS, Daxini SD (2021) Numerical analysis perspective in structural shape optimization: a review post 2000. Adv Eng Softw 155:102992

Vassberg J, Jameson A (2006) Aerodynamic shape optimization part 1: theoretical background. Introduction to optimization and multidisciplinary design, 1–30

Wazzan M, Abduljabbar A, Ajlan A, Ahmad R, Alhazmi T, Eskandar A, Khashoggi K, Alasadi F, Howladar S, Alshareef Y (2022) Reference for normal diameters of the abdominal aorta and common iliac arteries in the saudi population. Cureus 14(10)

Wilson NM, Arko FR, Taylor CA (2005) Predicting changes in blood flow in patient-specific operative plans for treating aortoiliac occlusive disease. Comput Aid Surg 10(4):257–277

Welker K (2016) Efficient pde constrained shape optimization in shape spaces. Phd thesis, Universität Trier,

Womersley JR (1955) Method for the calculation of velocity, rate of flow and viscous drag in arteries when the pressure gradient is known. J Physiol 127(3):553–563

Yakubov S, Cankurt B, Abdel-Maksoud M, Rung T (2013) Hybrid MPI/openMP parallelization of an Euler-Lagrange approach to cavitation modelling. Comput Fluids 80:365–371

Yu H, Engel S, Janiga G, Thévenin D (2017) A review of hemolysis prediction models for computational fluid dynamics. Artif Org 41(7):603–621

Yu H, Janiga G, Thévenin D (2016) Computational fluid dynamics-based design optimization method for archimedes screw blood pumps. Artif Org 40(4):341–352

Zander N, Bog T, Elhaddad M, Espinoza R, Hu H, Joly A, Wu C, Zerbe P, Düster A, Kollmannsberger S, Parvizian J, Ruess M, Schillinger D, Rank E (2014) FCMLab: a finite cell research toolbox for MATLAB. Adv Eng Softw 74:49–63

Zhang B, Liu X (2015) Topology optimization study of arterial bypass configurations using the level set method. Struct Multidisc Optim 51(3)

Zhang T, Taskin ME, Fang H-B, Pampori A, Jarvik R, Griffith BP, Wu ZJ (2011) Study of flow-induced hemolysis using novel Couette-type blood-shearing devices. Artif Org 35(12):1180–1186